39th AIAA Fluid Dynamics Conference
22 - 25 June 2009, San Antonio, Texas

AIAA Paper 2009-4041

Nonequilibrium and reactive high-speed flow simulations with a fifth-order WENO scheme

Xiaowen Wang* and Xiaolin Zhong #1
Mechanical and Aerospace Engineering Department
University of California, Los Angeles, CA 90095

Abstract

For high-speed flow over blunt bodies, gas temperature increases dramatically. As a result, gas molecules start dissociating, and vibration and electron energy modes are being excited. Gas becomes thermally nonequilibrium and chemically reactive. Effects of vibration and electron energy excitations, translation-vibration energy relaxation, and chemical reactions among different species need to be considered in numerical simulations. In current paper, a CFD solver based on a fifth-order WENO scheme is developed for the simulation of nonequilibrium and reactive high-speed flows, as part of the ADPDIS3D computer code package. The code is implemented based on a two-temperature model. It is assumed that translation and rotation energy modes are in equilibrium at the translation temperature whereas vibration and electron energy modes are in equilibrium at the vibration temperature. The code is validated and applied to numerical simulations of hypersonic nonequilibrium flows.

1. Introduction

Hypersonic flow is categorized by certain physical phenomena that do not typically play an important role in subsonic and supersonic flows. These effects could be thin shock layers, entropy layers, viscous-inviscid interactions due to the high displacement thickness of boundary layers, and high temperature gas effects [1].

At temperatures less then 500K-800K, gas flow stays calorically perfect. Only translation and rotation energy modes are fully excited while the excitations of vibration and electron energy modes and chemical reactions are negligible. As a result, specific heat capacities remain constant. When temperatures increase to 800K-2000K, vibration energy mode takes an important role in sharing the total energy with the translation and rotation modes. Near the lower temperature limit of this regime, translation-vibration energy relaxation between harmonic oscillator molecules dominates because most of the molecules are near the ground vibrational state. Near the higher limit of this regime, vibration-vibration energy relaxation becomes significantly active because not only are vibrationally excited molecules highly populated but also vibration-vibration energy relaxation is considerably faster than its translation-vibration counter-part. Also, the vibrational oscillation becomes inharmonic as the temperature approaches the dissociation level. However, results within the harmonic oscillator approximation are

* Postdoctoral researcher, Mechanical and Aerospace Engineering Department, UCLA, AIAA Member
# Professor, Mechanical and Aerospace Engineering Department, UCLA, AIAA Associate Fellow

known to be sufficiently accurate for most practical purposes [2]. For temperatures above 2000k-2500k, vibration energy mode is fully excited and O2 starts dissociating. Around 4000k, O2 is completely dissociated and N2 starts dissociating. When the temperature reaches 9000k, most of the N2 is dissociated. Coincidentally, this is the temperature around which the dissociated N and O atoms become ionized. Around 12000k, all the gases are completely dissociated and about 14% of them are ionized such that there is a sufficient amount of free charges, enough to make electromagnetic forces. Radiation emitted and absorbed by the gas can become important and could eventually modify the energy distribution in the flow field. At 20000k, double dissociation begins. And finally when it reaches 30000k, the gas is completely ionized [3]. These regimes correspond to M_∞ greater or much greater than 30.

All the high temperature gas effects are due to molecular collisions which occur at finite rates. When the collision rates are much faster than flow rates, it is called as "equilibrium flow". On the other hand, if the collision rates are much slower than flow rates, it is called as "frozen flow". Unfortunately, neither of these two situations can completely describe the hypersonic flow over a space/air vehicle. There will always be regions where the collision rates are in the same vicinity of the flow rates. Moreover different species will have different reaction rates and different energy relaxation rates. Therefore, energy transfers between bulk kinetic energy, translation energies, chemical energies, and vibration energies of different species are actively in progress at many locations in a hypersonic thermochemical nonequilibrium flow. When these effects start to play dominant roles, the flow is called "nonequilibrium flow".

In the past years, interest in various types of vehicles in hypersonic flow regime produced numerous structured grid based nonequilibrium flow solvers. According to recent publications, Laura, DPLR, and Lore are the most frequently referenced and are intensively validated against each other [4] and also against wind tunnel tests. LAURA (Langley Aerothermodynamic Upwind Relaxation Algorithm) is mainly developed by Peter Gnoffo et al. at the NASA Langley Research Center [5-8]. It uses Roe's flux difference splitting scheme with Yee's second-order symmetric total variation diminishing scheme to model the inviscid fluxes. Steady state solution is obtained using either point or line relaxation time integration scheme. The vibration energy mode is assumed to be in equilibrium with the electron energy, and translation energy is assumed to be in equilibrium with the rotation energy mode. The code supports multi-block structured grids and MPI communication for massive parallel computing.

DPLR (Data-Parallel Line Relaxation) is initially developed at University of Minnesota by Michael Wright and Graham Candler [9]. The code is further developed at NASA Ames research center [4]. DPLR implicit method is optimized for efficient parallel computing by arranging the body normal dependent data with local CPU in order to perform the relaxation process simultaneously in parallel mode. DPLR uses third order modified Steger-Warming flux splitting scheme with MUSCL data reconstruction to model the inviscid fluxes. Unlike LAURA, the vibration energy mode is separately treated, and translation energy is assumed to be equilibrium with the rotation and electron energy modes. It also supports multi-block structured grids.

Lore [10] was developed at the Advanced Operations and Engineering Services Group in Europe. The flow solver uses modified AUSM scheme with MUSCL data reconstruction to achieve second-order accuracy coupled with a van Albada limiter. Time advancement to a steady-state solution is achieved using an alternating direction line Gauss-Seidel implicit relaxation method. The code supports multi-block structured grids. This code covers a wide range of flight regimes from subsonic to hypersonic.

In current paper, a CFD solver based on a fifth-order WENO scheme is developed for the simulation of nonequilibrium and reactive high-speed flows. The solver is implemented to the ADPDIS3D computer code package developed mainly by Yee and Bjorn [11-17]. The code is based on a two-temperature model of Park [18]. It is assumed that translation and rotation energy modes are in equilibrium at the translation temperature whereas vibration and electron energy modes are in equilibrium at the vibration temperature. The flow solver uses the fifth-order WENO scheme of Jiang and Shu [19] with Roe's data reconstruction to model the inviscid fluxes. In order to validate the code, Yee's second-order total variation diminishing scheme is also implemented. Viscous fluxes are calculated by a sixth-order central scheme. Time integration of the governing equations is obtained using explicit Runge-Kutta method. The code is validated and applied to numerical simulations of hypersonic nonequilibrium flows.

2. Governing equations

2.1 Governing equations

For nonequilibrium and chemically reactive five species air flows, the governing equations are Navier-Stokes equations with source terms. Specifically, governing equations consist of five mass conservation equations, three momentum conservation equations, and two energy conservation equations, i.e.,

$$\frac{\partial \rho_s}{\partial t} + \frac{\partial}{\partial x_j}(\rho_s u_j) - \frac{\partial}{\partial x_j}(\rho D_s \frac{\partial y_s}{\partial x_j}) = \omega_s \tag{1}$$

$$\frac{\partial}{\partial t}(\rho u_i) + \frac{\partial}{\partial x_j}(\rho u_i u_j + p\delta_{ij}) - \frac{\partial}{\partial x_j}\left[\mu\left(\frac{\partial u_i}{\partial x_j} + \frac{\partial u_j}{\partial x_i}\right) - \frac{2}{3}\mu\frac{\partial u_k}{\partial x_k}\delta_{ij}\right] = 0 \tag{2}$$

$$\frac{\partial \rho E}{\partial t} + \frac{\partial}{\partial x_j}(\rho H u_j) - \frac{\partial}{\partial x_j}\left[u_i\mu\left(\frac{\partial u_i}{\partial x_j} + \frac{\partial u_j}{\partial x_i}\right) - \frac{2}{3}u_i\mu\frac{\partial u_k}{\partial x_k}\delta_{ij}\right] - \frac{\partial}{\partial x_j}\left(\rho\sum_{s=1}^{5} h_s D_s \frac{\partial y_s}{\partial x_j}\right) - \frac{\partial}{\partial x_j}\left(K\frac{\partial T}{\partial x_j} + K_V\frac{\partial T_V}{\partial x_j}\right) = 0 \tag{3}$$

$$\frac{\partial \rho e_V}{\partial t} + \frac{\partial}{\partial x_j}(\rho e_V u_j) - \frac{\partial}{\partial x_j}(\rho\sum_{s=1}^{3} e_{V,s} D_s \frac{\partial y_s}{\partial x_j}) - \frac{\partial}{\partial x_j}\left(K_V\frac{\partial T_V}{\partial x_j}\right) = \sum_{s=1}^{3}(Q_{T-V,s} + \omega_s e_{V,s}) \tag{4}$$

In above equations, D_s is diffusion coefficient of species, μ is viscosity of gas mixture, h_s is specific total enthalpy of species, K and K_V are heat conductivities relating to translation temperature and vibration temperature, e_V and $e_{V,s}$ are specific internal energies of gas mixture and species, $Q_{T-V,s}$ is energy relaxation, ω_s is the generation rate of diatomic species. y_s is the molar fraction of species, relating to mass fraction and molar mass as following,

$$y_s = \frac{(c_s/M_s)}{\sum_{i=1}^{5}(c_i/M_i)} \tag{5}$$

The other variables are defined as

$$\rho = \sum_{s=1}^{n}\rho_s \qquad p = \sum_{s=1}^{n} p_s \qquad p_s = \frac{\rho_s \bar{R} T}{M_s}$$

$$E = \frac{u_i u_i}{2} + \sum_{s=1}^{n}\frac{\rho_s e_s}{\rho} \qquad H = E + \frac{p}{\rho}$$

where $\bar{R}$ is the universal gas constant, e_s is specific internal energy of species.

2.2 Coordinate transform

The flow solver uses finite difference methods on structured grids. The following grid transform is applied to the governing equations.

$$\begin{cases} x = x(\xi,\eta,\zeta,\tau) \\ y = y(\xi,\eta,\zeta,\tau) \\ z = z(\xi,\eta,\zeta,\tau) \\ t = \tau \end{cases} \Leftrightarrow \begin{cases} \xi = \xi(x,y,z,t) \\ \eta = \eta(x,y,z,t) \\ \zeta = \zeta(x,y,z,t) \\ \tau = t \end{cases} \tag{6}$$

Jacobian matrix of the transform is,

$$J = \begin{vmatrix} x_\xi & y_\xi & z_\xi & 0 \\ x_\eta & y_\eta & z_\eta & 0 \\ x_\zeta & y_\zeta & z_\zeta & 0 \\ x_\tau & y_\tau & z_\tau & 1 \end{vmatrix} \tag{7}$$

With the transform relation, the governing equations in (ξ,η,ζ,τ) coordinate system can be written as

$$\frac{\partial(JU)}{\partial\tau} + \frac{\partial\tilde{F}_1}{\partial\xi} + \frac{\partial\tilde{F}_2}{\partial\eta} + \frac{\partial\tilde{F}_3}{\partial\zeta} + \frac{\partial\tilde{G}_1}{\partial\xi} + \frac{\partial\tilde{G}_2}{\partial\eta} + \frac{\partial\tilde{G}_3}{\partial\zeta} = JS \tag{8}$$

Where

$$\tilde{F}_1 = J\xi_x F_1 + J\xi_y F_2 + J\xi_z F_3 + JU\xi_t$$

$$\tilde{F}_2 = J\eta_x F_1 + J\eta_y F_2 + J\eta_z F_3 + JU\eta_t$$
$$\tilde{F}_3 = J\zeta_x F_1 + J\zeta_y F_2 + J\zeta_z F_3 + JU\zeta_t$$
$$\tilde{G}_1 = J\xi_x G_1 + J\xi_y G_2 + J\xi_z G_3$$
$$\tilde{G}_2 = J\eta_x G_1 + J\eta_y G_2 + J\eta_z G_3$$
$$\tilde{G}_3 = J\zeta_x G_1 + J\zeta_y G_2 + J\zeta_z G_3$$

The corresponding fluxes (inviscid & viscous) and source terms are also written in matrix form as

$$F_j = \begin{pmatrix} \rho_1 u_j \\ \rho_2 u_j \\ \rho_3 u_j \\ \rho_4 u_j \\ \rho_5 u_j \\ \rho u u_j + p\delta_{1j} \\ \rho v u_j + p\delta_{2j} \\ \rho w u_j + p\delta_{3j} \\ \rho H u_j \\ \rho e_V u_j \end{pmatrix} \quad G_j = \begin{pmatrix} \rho_1 v_{1j} \\ \rho_2 v_{2j} \\ \rho_3 v_{3j} \\ \rho_4 v_{4j} \\ \rho_5 v_{5j} \\ -\tau_{1j} \\ -\tau_{2j} \\ -\tau_{3j} \\ -u_i\tau_{ij} + q_j + q_{Vj} + \sum_{s=1}^{5} \rho_s h_s v_{sj} \\ q_{Vj} + \sum_{s=1}^{3} \rho_s e_{V,s} v_{sj} \end{pmatrix} \quad S = \begin{pmatrix} \omega_1 \\ \omega_2 \\ \omega_3 \\ \omega_4 \\ \omega_5 \\ 0 \\ 0 \\ 0 \\ 0 \\ \sum_{s=1}^{3} (Q_{T-V,s} + \omega_s e_{V,s}) \end{pmatrix}$$

In above equations, $v_{sj} = u_{sj} - u_j$ is diffusion velocity of species s.

3. Numerical methods

For the thermally non-equilibrium and chemically reacting system (8) in the direction, $\mathrm{k} = (k_1, k_2, k_3)$, the corresponding inviscid flux term is

$$\mathrm{F} = \begin{pmatrix} \rho_1 \,\mathrm{k\,u} \\ \rho_2 \,\mathrm{k\,u} \\ \rho_3 \,\mathrm{k\,u} \\ \rho_4 \,\mathrm{k\,u} \\ \rho_5 \,\mathrm{k\,u} \\ \rho u \,\mathrm{k\,u} + p k_1 \\ \rho v \,\mathrm{k\,u} + p k_2 \\ \rho w \,\mathrm{k\,u} + p k_3 \\ \rho H \,\mathrm{k\,u} \\ \rho e_V \,\mathrm{k\,u} \end{pmatrix} \tag{9}$$

The Jacobian matrix of inviscid flux is defined as,

$$\mathrm{A} = \frac{\partial \mathrm{F}}{\partial \mathrm{U}} = L\Lambda R \tag{10}$$

Where,

$$A = |\mathrm{k}| \begin{bmatrix} \tilde{U}(\delta_{sr} - c_s) & c_s n_x & c_s n_y & c_s n_z & 0 & 0 \\ \tilde{\gamma}_r n_x - \tilde{U}u & -\beta u n_x + u n_x + \tilde{U} & -\beta v n_x + u n_y & -\beta w n_x + u n_z & \beta n_x & \phi n_x \\ \tilde{\gamma}_r n_y - \tilde{U}v & -\beta u n_y + v n_x & -\beta v n_y + v n_y + \tilde{U} & -\beta w n_y + v n_z & \beta n_y & \phi n_y \\ \tilde{\gamma}_r n_z - \tilde{U}w & -\beta u n_z + w n_x & -\beta v n_z + w n_y & -\beta w n_z + w n_z + \tilde{U} & \beta n_z & \phi n_z \\ \tilde{\gamma}_r \tilde{U} - \tilde{U}H & -\beta u \tilde{U} + H n_x & -\beta v \tilde{U} + H n_y & -\beta w \tilde{U} + H n_z & \beta \tilde{U} + \tilde{U} & \phi \tilde{U} \\ -\tilde{U} e_V & e_V n_x & e_V n_y & e_V n_z & 0 & \tilde{U} \end{bmatrix}$$

$$R = \begin{bmatrix} a^2 \delta_{sr} - c_s \tilde{\gamma}_r & \beta u c_s & \beta v c_s & \beta w c_s & -\beta c_s & -\phi c_s \\ -\tilde{V} & l_x & l_y & l_z & 0 & 0 \\ -\tilde{W} & m_x & m_y & m_z & 0 & 0 \\ \tilde{\gamma}_r - \tilde{U}a & a n_x - \beta u & a n_y - \beta v & a n_z - \beta w & \beta & \phi \\ \tilde{\gamma}_r + \tilde{U}a & -a n_x - \beta u & -a n_y - \beta v & -a n_z - \beta w & \beta & \phi \\ -e_V \tilde{\gamma}_r & \beta u e_V & \beta v e_V & \beta w e_V & -\beta e_V & a^2 - \phi e_V \end{bmatrix}$$

$$L = \begin{bmatrix} \delta_{sr}/a^2 & 0 & 0 & c_s/2a^2 & c_s/2a^2 & 0 \\ u/a^2 & l_x & m_x & (u + a n_x)/2a^2 & (u - a n_x)/2a^2 & 0 \\ v/a^2 & l_y & m_y & (v + a n_y)/2a^2 & (v - a n_y)/2a^2 & 0 \\ w/a^2 & l_z & m_z & (w + a n_z)/2a^2 & (w - a n_z)/2a^2 & 0 \\ \left[\beta(u^2 + v^2 + w^2) - \tilde{\gamma}_r\right]/\beta a^2 & \tilde{V} & \tilde{W} & (H + a\tilde{U})/2a^2 & (H - a\tilde{U})/2a^2 & -\phi/\beta a^2 \\ 0 & 0 & 0 & e_V/2a^2 & e_V/2a^2 & 1/a^2 \end{bmatrix}$$

All three matrices are obtained from Gnoffo et al.'s report [20]. Subscript "s" refers to row s and species s whereas subscript "r" refers to column r and species r. Both s and r vary from 1 to 5 in the present model. The unit vector n is defined from vector k as

$$\mathrm{n} = (n_x, n_y, n_z) = \frac{(k_1, k_2, k_3)}{|\mathrm{k}|}$$

$\mathrm{l} = (l_x, l_y, l_z)$ and $\mathrm{m} = (m_x, m_y, m_z)$ are two unit vectors such that n, l, and m are mutually orthogonal.

$$\tilde{U} = u n_x + v n_y + w n_z$$
$$\tilde{V} = u l_x + v l_y + w l_z$$

$$\tilde{W} = um_x + vm_y + wm_z$$

The eigenvalues of Jacobian matrix (10) are

$$\lambda_{1,2,3,4,5,6,7,10} = |\mathrm{k}|\tilde{U} \tag{11}$$

$$\lambda_8 = |\mathrm{k}|(\tilde{U} + a) \tag{12}$$

$$\lambda_9 = |\mathrm{k}|(\tilde{U} - a) \tag{13}$$

The derivative of pressure respecting to conservative variables comes from

$$dp = \beta(d\rho E - ud\rho u - vd\rho v - wd\rho w) + \phi d\rho e_V + \tilde{\gamma}_s d\rho_s \tag{14}$$

Where

$$\beta = \frac{\bar{R}}{\rho \sum_s c_s c_{v,tr}^s} \sum_{r=1}^{5} \frac{\rho_r}{M_r} \tag{15}$$

$$\phi = -\beta \tag{16}$$

$$\tilde{\gamma}_s = \frac{\bar{R}T}{M_s} + \beta \frac{u^2 + v^2 + w^2}{2} - \beta e_s - \phi e_{V,s} \tag{17}$$

$$a^2 = \sum_{s=1}^{5} c_s \tilde{\gamma}_s + \beta\left[H - (u^2 + v^2 + w^2)\right] + \phi e_V \tag{18}$$

Suppose the numerical scheme can be written as,

$$\mathrm{U}_{i,j,k}^{n+1} = \mathrm{U}_{i,j,k}^{n} - \frac{\Delta t}{\Delta \xi}\left(\tilde{\mathrm{F}}_{i+1/2}^{n} - \tilde{\mathrm{F}}_{i-1/2}^{n}\right) + \cdots \tag{19}$$

The flux terms can be obtained by fifth-order WENO scheme or second-order TVD scheme. Details of the flux calculation are discussed below.

3.1 Jiang-Shu fifth-order WENO scheme

For the CFD solver developed in current paper, the fifth-order WENO scheme of Jiang and Shu [19] is used for inviscid fluxes as shown in Eq. (9). At first, the flux can split into two parts with the global Lax-Friedrichs splitting, i.e.,

$$\tilde{F}^{\pm} = \frac{1}{2}\left(\tilde{F} \pm \alpha U\right) \tag{20}$$

where α is the maximum eigenvalue of the Jacobian matrix.

In the paper, only the computation of the positive part of split flux is described. The formulas for the negative part are symmetric. Here the flux version of ENO scheme is used as the basis to formulate WENO scheme.

$$\tilde{\mathrm{F}}_{i+1/2} = \sum_{k=0}^{2} \omega_k q_k^3 \left(\mathrm{F}_{i+k-2}, \mathrm{F}_{i+k-1}, \mathrm{F}_{i+k} \right) \tag{21}$$

Where q_k^3 is the flux version of ENO scheme on the kth candidate stencil, i.e.,

$$q_k^3(g_0, g_1, g_2) = \sum_{l=0}^{2} a_{k,l}^3 g_l \tag{22}$$

In Eq. (21), the weight ω_k is defined by

$$\omega_k = \frac{\alpha_k}{\alpha_0 + \alpha_1 + \alpha_2} \tag{23}$$

$$\alpha_k = \frac{C_k^3}{(\varepsilon + IS_k)^2} \tag{24}$$

In above equation, IS_k is a smoothness measurement of the numerical flux on the kth candidate stencil. As shown in Jiang and Shu's paper,

$$IS_k = \frac{1}{2}\left(\left(F\left[j+k-2, 1 \right] \right)^2 + \left(F\left[j+k-1, 1 \right] \right)^2 + \left(F\left[j+k-2, 2 \right] \right)^2 \right) \tag{25}$$

where $F\left[\cdot, l\right]$ is the lth undivided difference. All the parameters in Eqs. (22) and (24) are obtained from Jiang and Shu's paper.

3.2 Harten-Yee second-order TVD scheme

In order to validate the code, Yee's second-order total variation diminishing (TVD) scheme is also implemented [21]. The flux term can be obtained as following,

$$\tilde{\mathrm{F}}_{i+1/2} = \frac{1}{2}\left[\mathrm{F}_{i+1,j,k} + \mathrm{F}_{i,j,k} + \mathrm{R}_{i+1/2}\, \Phi_{i+1/2} \right] \tag{26}$$

$$\mathrm{R}_{i+1/2} = \mathrm{R}\left(\mathrm{U}_{i+1/2} \right) \tag{27}$$

$$\Phi_{i+1/2}^l = \frac{1}{2} Q\left(a_{i+1/2}^l \right) \left[g_{i+1}^l + g_i^l \right] - Q\left(a_{i+1/2}^l + \gamma_{i+1/2}^l \right) \alpha_{i+1/2}^l \tag{28}$$

$$\gamma_{i+1/2}^l = \frac{1}{2} Q\left(a_{i+1/2}^l \right) \frac{\alpha_{i+1/2}^l \left(g_{i+1}^l - g_i^l \right)}{\left(\alpha_{i+1/2}^l \right)^2 + 1.0^{-10}} \tag{29}$$

With

$$Q(x) = \sqrt{x^2 + \varepsilon^2} \tag{30}$$

The parameter is defined relating to the velocity. The fluxes in other dimensions are similarly treated in a dimension-by-dimension manner.

In equations (28) to (30), a^l is the l th eigenvalue of A , α^l is the jump in the characteristic variables corresponding to l th eigenvalue, g is flux limiter. All these variables are determined by approximate Riemann solver.

$$\alpha = R(\mathrm{U}^R - \mathrm{U}^L) \tag{31}$$

3.3 Roe's data reconstruction

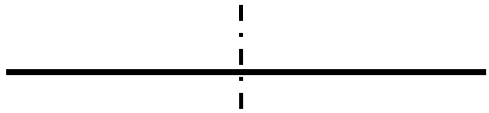

Roe's data reconstruction of the inviscid fluxes is used together with the fifth-order WENO scheme and the second-order TVD scheme. As shown in above schematic, variables at i+1/2 computed by,

$$\overline{\rho}_i = \frac{\rho_{iL}\sqrt{\rho_{iR}} + \rho_{iR}\sqrt{\rho_{iL}}}{\sqrt{\rho_{iL}} + \sqrt{\rho_{iR}}} = \sqrt{\rho_{iL}\rho_{iR}} \tag{32}$$

$$\overline{\mathrm{u}} = \frac{\mathrm{u}_L\sqrt{\rho_L} + \mathrm{u}_R\sqrt{\rho_R}}{\sqrt{\rho_L} + \sqrt{\rho_R}} \tag{33}$$

$$\overline{H} = \frac{H_L\sqrt{\rho_L} + H_R\sqrt{\rho_R}}{\sqrt{\rho_L} + \sqrt{\rho_R}} \tag{34}$$

$$\overline{c}_s = \frac{c_{s,L}\sqrt{\rho_L} + c_{s,R}\sqrt{\rho_R}}{\sqrt{\rho_L} + \sqrt{\rho_R}} \tag{35}$$

$$\overline{e} = \frac{e_L\sqrt{\rho_L} + e_R\sqrt{\rho_R}}{\sqrt{\rho_L} + \sqrt{\rho_R}} \tag{36}$$

$$\overline{T} = \frac{T_L\sqrt{\rho_L} + T_R\sqrt{\rho_R}}{\sqrt{\rho_L} + \sqrt{\rho_R}} \tag{37}$$

4 Nonequilibrium models

4.1 Models of vibration and electron energy

Three models of vibration and electron energy are implemented in the code. In Candler's model [22], vibration energy and electron energy are considered separately with different formula. While in Gnoffo et al.'s model [20] and McBride & Gordon's model [23], vibration and electron energy are calculated together from the curve fits of experimental correlations. The difference between these three models comes from how they evaluate specific total enthalpy of species and specific heat in constant pressure of species.

In Candler's model, specific total enthalpy of species and specific heat in constant pressure of species are defined as,

$$h_s = c_{vs}T + \frac{p_s}{\rho_s} + E_V + h_s^0 \tag{38}$$

$$c_p^s = c_v^s + \frac{\bar{R}}{M_s} + c_V^s \tag{39}$$

where h_s^0 is the generation enthalpy of species. The variables on the right hand side of equations (38) and (39) are calculated from the following formula,

$$E_V = (e_v + e_{els}) = \sum_{s=1}^{3} \frac{\bar{R}}{M_s}\left(\frac{\theta_{vs}}{e^{\theta_{vs}/T_V} - 1} + \frac{g_{1s}\theta_{els}\exp(-\theta_{els}/T_V)}{g_{0s} + g_{1s}\exp(-\theta_{elis}/T_V)} \right)$$

$$c_v^s = c_{vtr,s} + c_{vrot,s} \quad c_{vtr,s} = \frac{3\bar{R}}{2M_s} \qquad c_{vrot,s} = \begin{cases} \dfrac{\bar{R}}{M_s} & (s = 1,3) \\ 0 & (otherwise) \end{cases}$$

$$c_V^s = \frac{\bar{R}}{M_s}\left(\frac{(\theta_{vs}/T_V)^2 e^{\theta_{vs}/T_V}}{\left(e^{\theta_{vs}/T_V} - 1\right)^2} + \frac{g_{0s}g_{1s}(\theta_{els}/T_V)^2 \exp(-\theta_{els}/T_V)}{\left(g_{0s} + g_{1s}\exp(-\theta_{elis}/T_V)\right)^2} \right)$$

The related parameters are listed in Table 1.

Table 1. Parameters used in Candler's model

Species	h_s^0 (J/kg)	M_s (g)	θ_{vs} (K)	θ_{els} (K)	g_0	g_1
N2	0	28	3395	-	-	-
O2	0	32	2239	11341	3	2
NO	2.996123e6	30	2817	-	-	-
N	3.362161e7	14	-	27665	9	10
O	1.543119e7	16	-	22831	9	5

In Gnoffo et al.'s model, specific total enthalpy of species and specific heat in constant pressure of species are defined as,

$$h_s(T, T_V) = (c_{p,t}^s + c_{p,r}^s)(T - T_V) + h_s(T_V) \tag{40}$$

$$c_p^s(T) = \frac{\bar{R}}{M_s}\sum_{k=1}^{5} A_k^s T^{k-1} \tag{41}$$

where $h_s(T_V) = \dfrac{\bar{R}}{M_s}\left(\sum_{k=1}^{5} \dfrac{A_k^s T_V^k}{k} + A_6^s \right)$.

Parameters of the curve fit are listed in Table 2. With the temperature increasing from 300 K to 35000 K, five sets of curve fits are employed for different temperature range,

1. $300 \le T \le 1000$ 2. $1000 \le T \le 6000$ 3. $6000 \le T \le 15000$
4. $15000 \le T \le 25000$ 5. $25000 \le T \le 35000$

Table 2. curve fit parameters in Gnoffo et al.'s model

Species	Range	A_1	A_2	A_3	A_4	A_5	A_6
N2	1	3.674826	-1.208150e-3	2.324010e-6	- 6.321755e-10	- 2.257725e-13	- 1061.16
	2	2.896319	1.515486e-3	- 5.723527e-7	9.980739e-11	- 6.522355e-15	- 905.862
	3	3.727	4.684e-4	- 1.140e-7	1.154e-11	- 3.293e-16	- 1043.00
	4	9.637690	- 2.572840e-3	3.301980e-7	- 1.431490e-11	2.033260e-16	- 1043.00
	5	- 5.168080	2.333690e-3	- 1.295340e-7	2.787210e-12	- 2.135960e-17	- 1043.00
O2	1	3.625598	- 1.878218e-3	7.055454e-6	- 6.763513e-9	2.155599e-12	- 1047.52
	2	3.621953	7.361826e-4	- 1.965222e-7	3.620155e-11	- 2.894562e-15	- 1201.98
	3	3.721	4.254e-4	- 2.835e-8	6.050e-13	- 5.186e-18	- 1044.00
	4	3.486660	5.238420e-4	- 3.912340e-8	1.009350e-12	- 8.871830e-18	- 1044.00
	5	3.961980	3.944550e-4	- 2.950580e-8	7.397450e-13	- 6.420930e-18	- 1044.00
NO	1	4.045952	- 3.418178e-3	7.981919e-6	- 6.113931e-9	1.591907e-12	9745.39
	2	3.189	1.338228e-3	- 5.289932e-7	9.591933e-11	- 6.484793e-15	9828.33
	3	3.845	2.521e-4	- 2.658e-8	2.162e-12	- 6.381e-17	9764.00
	4	4.330870	- 5.808630e-5	2.805950e-8	- 1.569410e-12	2.410390e-17	9764.00
	5	2.350750	5.864300e-4	- 3.131650e-8	6.049510e-13	- 4.055670e-18	9764.00
N	1	2.503071	- 2.180018e-5	5.420528e-8	- 5.647560e-11	2.099904e-14	56098.9
	2	2.450268	1.066145e-4	- 7.465337e-8	1.879652e-11	- 1.025983e-15	56116.0
	3	2.748	- 3.909e-4	1.338e-7	- 1.191e-11	3.369e-16	56090.0
	4	- 1.227990	1.926850e-3	- 2.437050e-7	1.219300e-11	- 1.991840e-16	56090.0
	5	15.52020	- 3.885790e-3	3.228840e-7	- 9.605270e-12	9.547220e-17	56090.0
O	1	2.946428	- 1.638166e-3	2.421031e-6	- 1.602843e-9	3.890696e-13	29147.6
	2	2.542059	- 2.755061e-5	- 3.102803e-9	4.551067e-12	- 4.368051e-16	29230.8
	3	2.548	- 5.952e-5	2.701e-8	- 2.798e-12	9.380e-17	29150.0
	4	- 9.787120e-3	1.244970e-3	- 1.615440e-7	8.037990e-12	- 1.262400e-16	29150.0
	5	16.42810	- 3.931300e-3	2.983990e-7	- 8.161280e-12	7.500430e-17	29150.0

In McBride and Gordon's model, specific total enthalpy of species and specific heat in constant pressure of species are defined as,

$$\frac{h_s\left(T,T_V\right)}{RT} = -a_{1s}\frac{1}{T^2} + a_{2s}\frac{\ln(T)}{T} + a_{3s} + a_{4s}\frac{T}{2} + a_{5s}\frac{T^2}{3} + a_{6s}\frac{T^3}{4} + a_{7s}\frac{T^4}{5} + b_{1s}\frac{1}{T} \qquad (42)$$

$$\frac{c_p^s}{R} = a_{1s}\frac{1}{T^2} + a_{2s}\frac{1}{T} + a_{3s} + a_{4s}T + a_{5s}T^2 + a_{6s}T^3 + a_{7s}T^4 \qquad (43)$$

Parameters of the curve fit are listed in Tables 3 to 7 for each species.

Table 3. Curve fit parameters for N2 in MaBride & Gordon's model

Parameter	200 – 1000 K	1000 – 6000 K	6000 – 20000 K
a_{1s}	2.210371497×10^{4}	5.877124060×10^{5}	8.31013916×10^{8}
a_{2s}	-3.818461820×10^{2}	-2.239249073×10^{3}	-6.42073354×10^{5}
a_{3s}	6.082738360	6.066949220	2.020264635×10^{2}
a_{4s}	$-8.530914410\times10^{-3}$	$-6.139685500\times10^{-4}$	$-3.065092046\times10^{-2}$
a_{5s}	1.384646189×10^{-5}	1.491806679×10^{-7}	2.486903333×10^{-6}
a_{6s}	$-9.625793620\times10^{-9}$	$-1.923105485\times10^{-11}$	$-9.705954110\times10^{-11}$
a_{7s}	$2.519705809\times10^{-12}$	$1.061954386\times10^{-15}$	$1.437538881\times10^{-15}$
b_{1s}	7.108460860×10^{2}	1.283210415×10^{4}	4.938707040×10^{6}

Table 4. Curve fit parameters for O2 in MaBride & Gordon's model

Parameter	200 – 1000 K	1000 – 6000 K	6000 – 20000 K
a_{1s}	-3.425563420×10^{4}	-1.037939022×10^{6}	4.975294300×10^{8}
a_{2s}	4.847000970×10^{2}	2.344830282×10^{3}	-2.866106874×10^{5}
a_{3s}	1.119010961	1.819732036	6.690352250×10^{1}
a_{4s}	4.293889240×10^{-3}	1.267847582×10^{-3}	$-6.169959020\times10^{-3}$
a_{5s}	$-6.836300520\times10^{-7}$	$-2.188067988\times10^{-7}$	3.016396027×10^{-7}
a_{6s}	$-2.023372700\times10^{-9}$	$2.053719572\times10^{-11}$	$-7.421416600\times10^{-12}$
a_{7s}	$1.039040018\times10^{-12}$	$-8.193467050\times10^{-16}$	$7.278175770\times10^{-17}$
b_{1s}	-3.391454870×10^{3}	-1.689010929×10^{4}	2.293554027×10^{6}

Table 5. Curve fit parameters for NO in MaBride & Gordon's model

Parameter	200 – 1000 K	1000 – 6000 K	6000 – 20000 K
a_{1s}	-1.143916503×10^{4}	2.239018716×10^{5}	-9.575303540×10^{8}
a_{2s}	1.536467592×10^{2}	-1.289651623×10^{3}	5.912434480×10^{5}
a_{3s}	3.431468730	5.433936030	-1.384566826×10^{2}
a_{4s}	$-2.668592368\times10^{-3}$	$-3.656034900\times10^{-4}$	1.694339403×10^{-2}
a_{5s}	8.481399120×10^{-6}	9.880966450×10^{4}	$-1.007351096\times10^{-6}$
a_{6s}	$-7.685111050\times10^{-9}$	$-1.416076856\times10^{-11}$	$2.912584076\times10^{-11}$
a_{7s}	$2.386797655\times10^{-12}$	$9.380184620\times10^{-16}$	$-3.295108350\times10^{-16}$
b_{1s}	9.098214410×10^{3}	1.750317656×10^{4}	-4.677501240×10^{6}

Table 6. Curve fit parameters for N in MaBride & Gordon's model

Parameter	200 – 1000 K	1000 – 6000 K	6000 – 20000 K
a_{1s}	2.5	8.876501380×10^{4}	5.475181050×10^{8}
a_{2s}	0	-1.071231500×10^{2}	-3.107574980×10^{5}
a_{3s}	0	2.362188287	6.91678274×10^{1}
a_{4s}	0	2.916720081×10^{-4}	$-6.847988130\times10^{-3}$
a_{5s}	0	$-1.729515100\times10^{-7}$	3.827572400×10^{-7}
a_{6s}	0	$4.012657880\times10^{-11}$	$-1.098367709\times10^{-11}$
a_{7s}	0	$-2.677227571\times10^{-15}$	$1.277986024\times10^{-16}$
b_{1s}	5.610463780×10^{4}	5.697351330×10^{4}	2.550585618×10^{6}

Table 7. Curve fit parameters for O in MaBride & Gordon's model

Parameter	200 – 1000 K	1000 – 6000 K	6000 – 20000 K
a_{1s}	-7.953611300×10^{3}	2.619020262×10^{5}	1.779004264×10^{8}
a_{2s}	1.607177787×10^{2}	-7.298722030×10^{2}	-1.082328257×10^{5}
a_{3s}	1.966226438	3.317177270	2.810778365×10^{1}
a_{4s}	1.013670310×10^{-3}	$-4.281334360\times10^{-4}$	-2.97532262×10^{-3}
a_{5s}	$-1.110415423\times10^{-6}$	1.036104594×10^{-7}	1.854997534×10^{-7}
a_{6s}	$6.517507500\times10^{-10}$	$-9.438304330\times10^{-12}$	$-9.438304330\times10^{-12}$
a_{7s}	$-1.584779251\times10^{-13}$	$2.725038297\times10^{-16}$	$2.725038297\times10^{-16}$
b_{1s}	2.840362437×10^{4}	3.392428060×10^{4}	8.89094263×10^{5}

Comparisons of vibration and electron energy (E_V) and its corresponding specific heat in constant volume (c_V) for each species are shown in figs. 1 to 5.

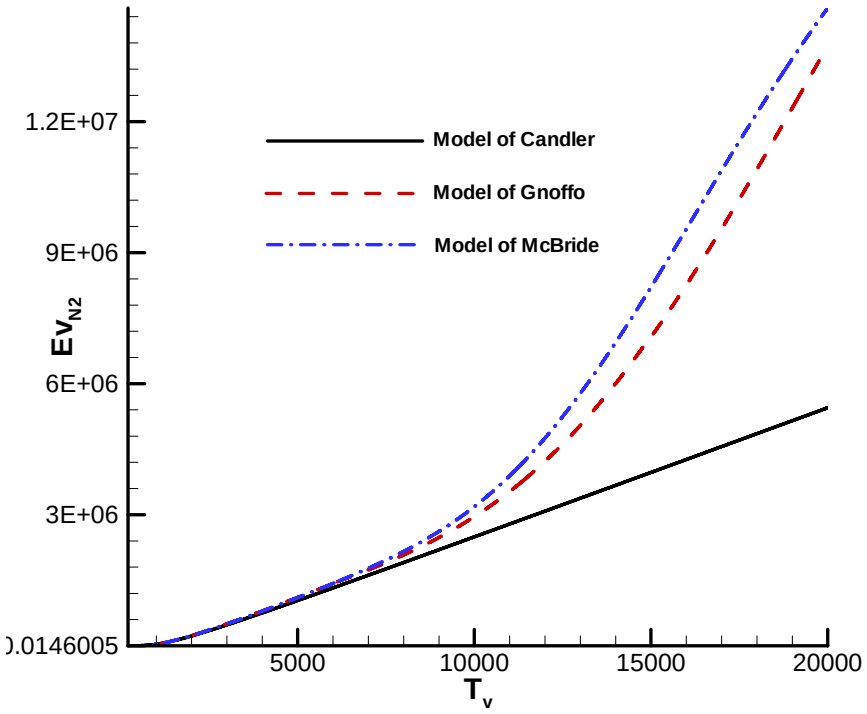

a)

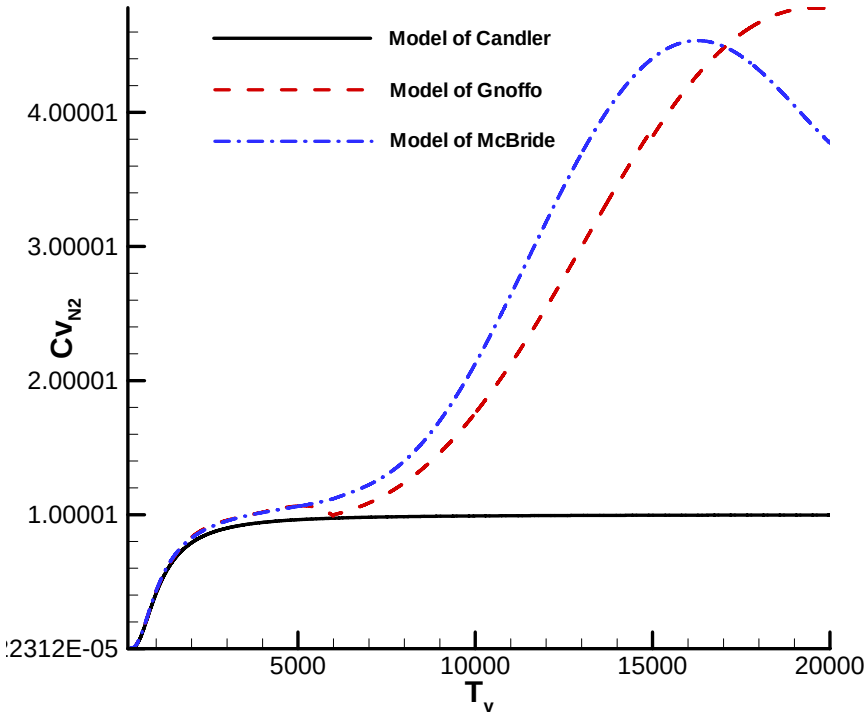

b)

Figure 1. vibration & electron energy and corresponding specific heat in constant volume of N2

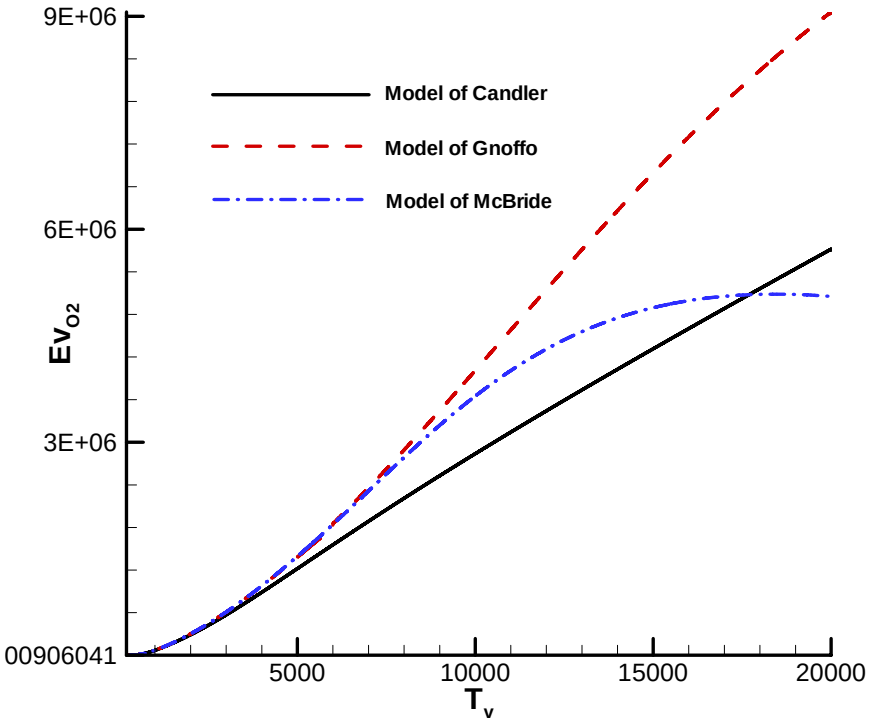

a)

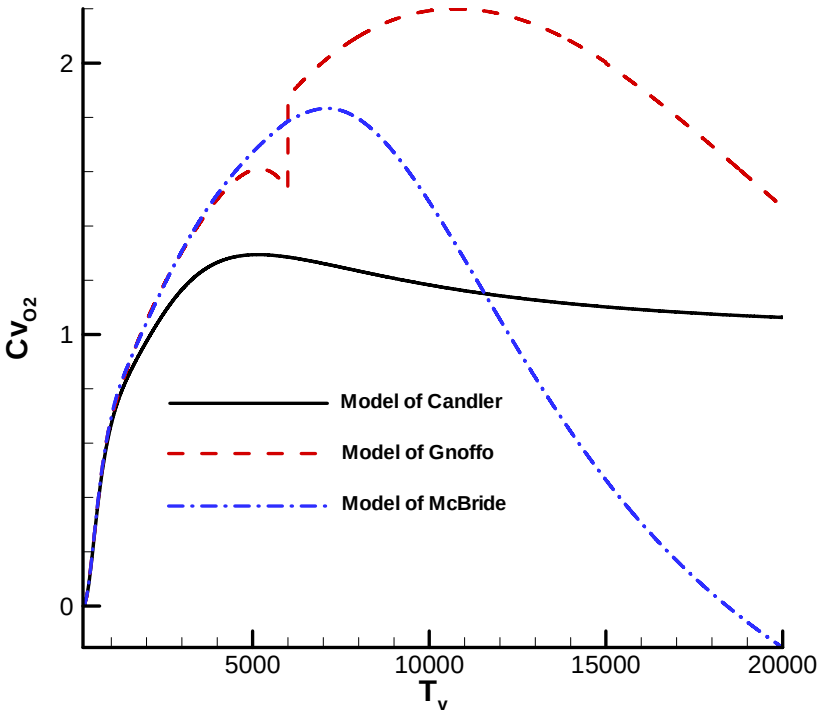

b)

Figure 2. vibration & electron energy and corresponding specific heat in constant volume of O2

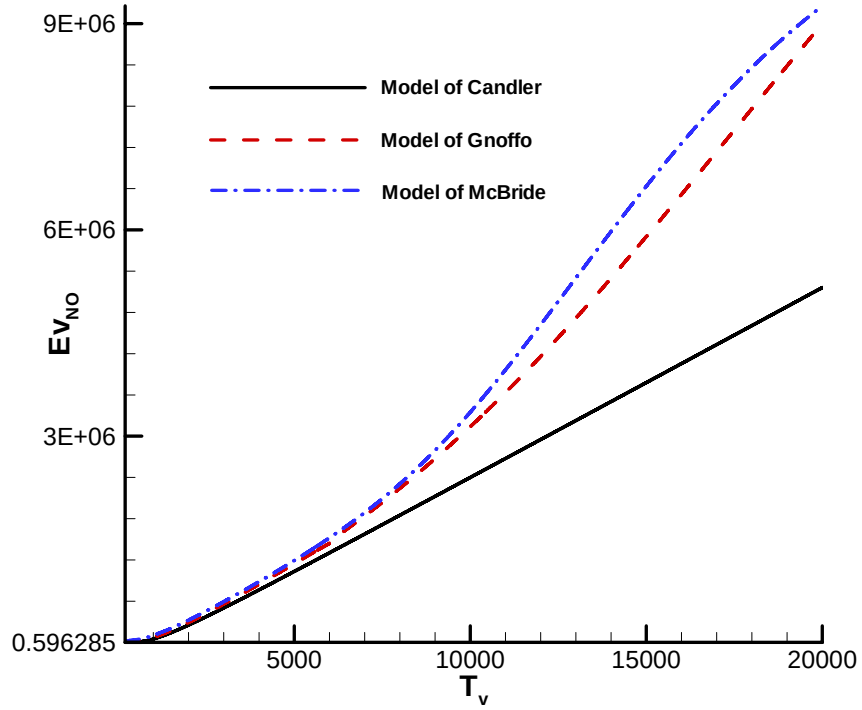

a)

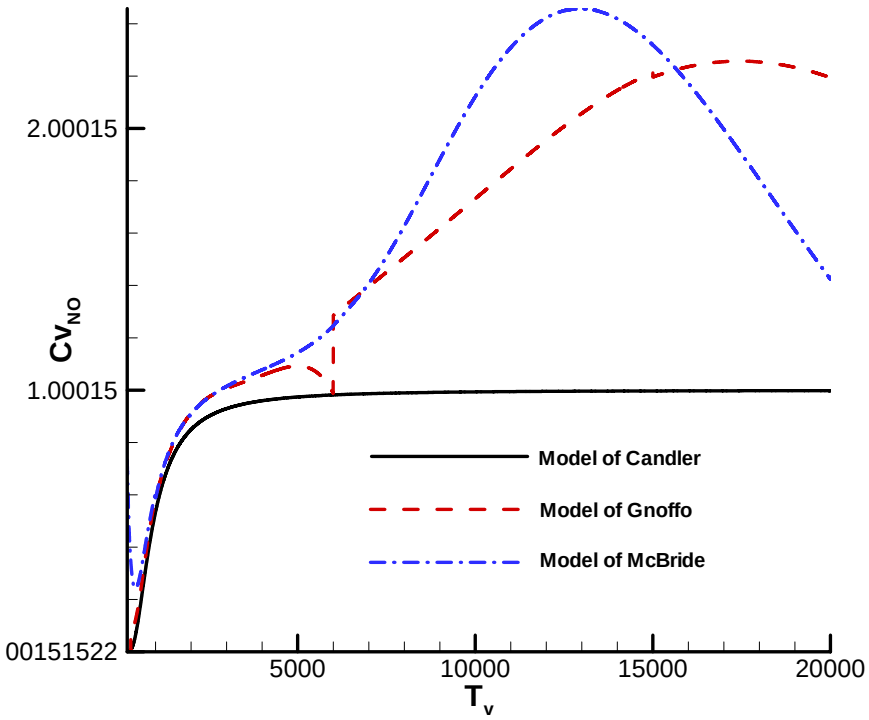

b)

Figure 3. vibration & electron energy and corresponding specific heat in constant volume of NO

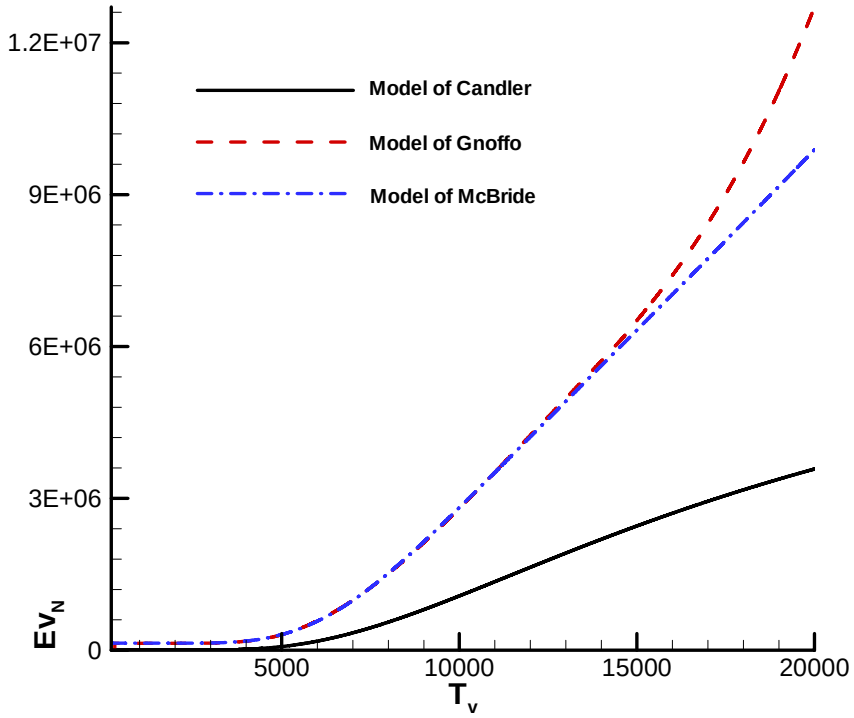

a)

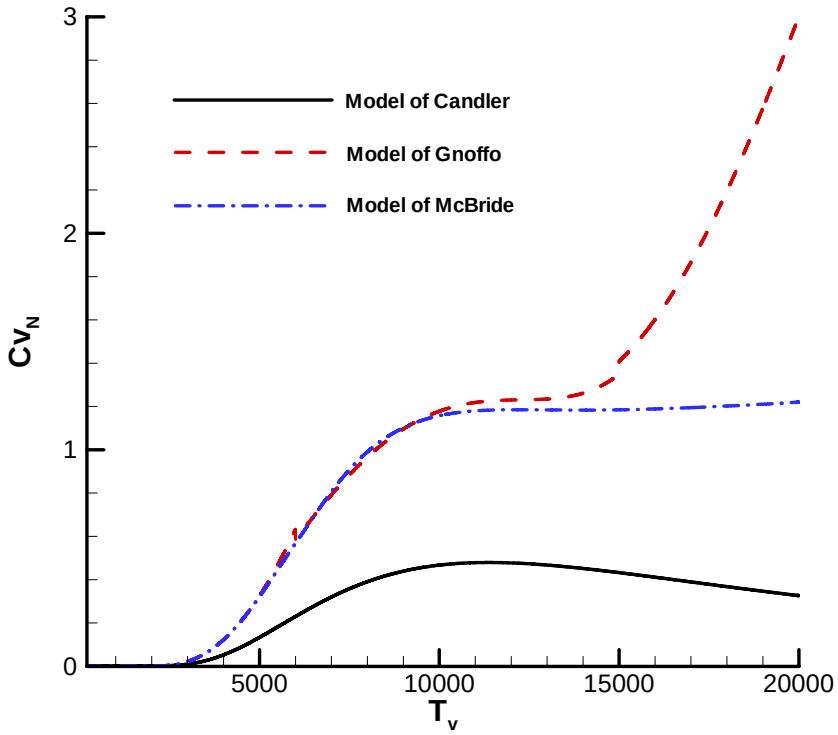

b)

Figure 4. vibration & electron energy and corresponding specific heat in constant volume of N

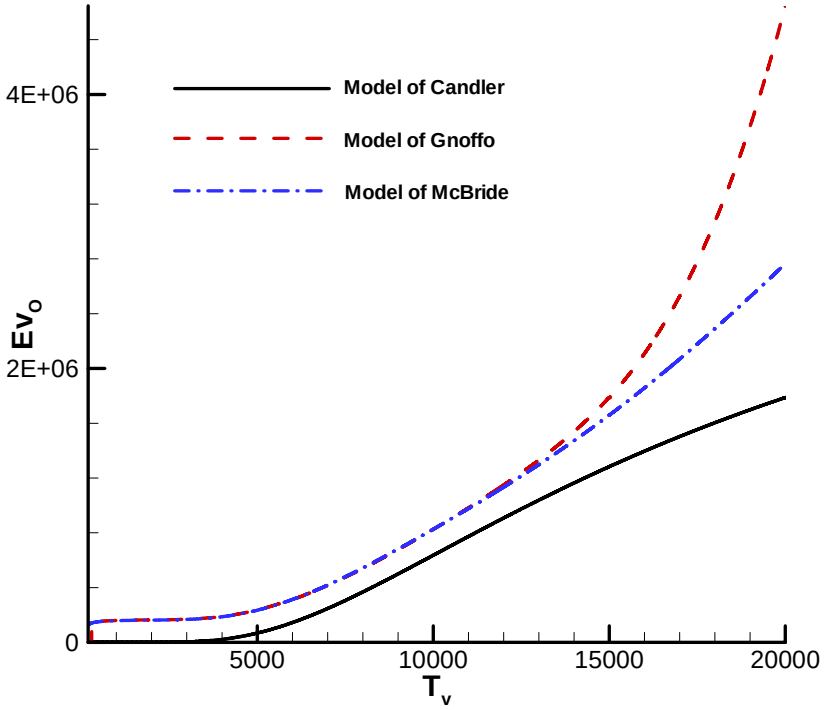

a)

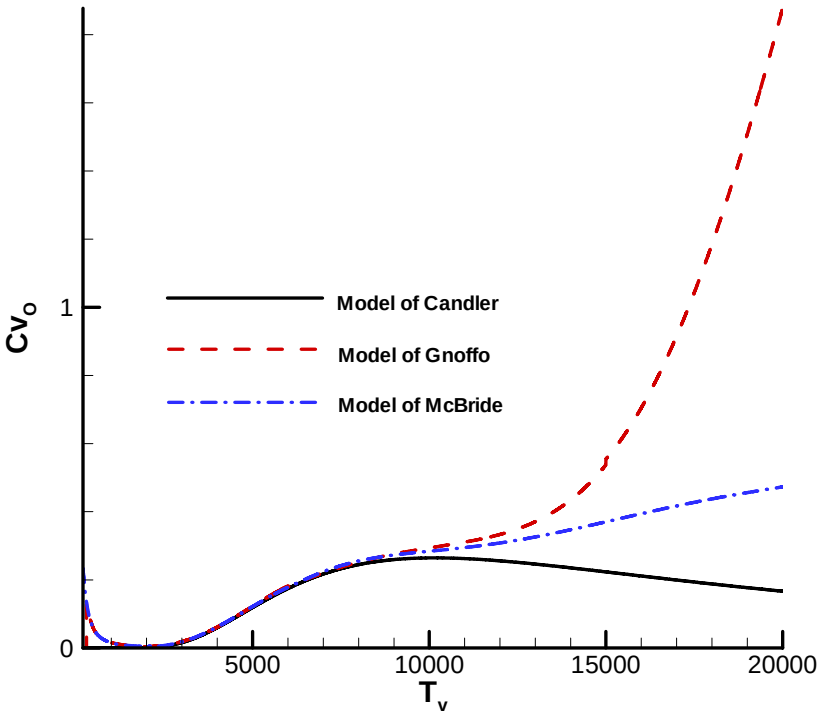

b)

Figure 5. vibration & electron energy and corresponding specific heat in constant volume of O

Figures 1 to 5 show that electron energy mode is quite significant when the vibration temperature increase to around 10,000 K.

4.2 Thermal properties

The viscosity of each species is calculated from the following curve fits. For the five species considered in current code, coefficients of curve fits are listed in Table 8, with the original data being obtained from Candler's dissertation [22].

$$\mu_s = 0.1\exp\left[(A_s \ln T + B_s)\ln T + C_s\right] \tag{44}$$

Table 8. Curve fit coefficients of species viscosity

Species	N2	O2	NO	N	O
A_s	0.0268142	0.0449290	0.0436378	0.0115572	0.0203144
B_s	0.3177838	-0.0826158	-0.0335511	0.6031679	0.4294404
C_s	-11.3155513	-9.2019475	-9.5767430	-12.4327495	-11.6031403

By combining the viscosity of each species, the total viscosity is calculated as

$$\mu = \sum_{s=1}^{5} \frac{y_s \mu_s}{\phi_s} \tag{45}$$

Heat conductivities of each species corresponding to translation temperature and vibration temperature are calculated as

$$\kappa_s = \mu_s\left(\frac{5}{2}c_{vtr,s} + c_{vrot,s}\right) \tag{46}$$

$$\kappa_{Vs} = \mu_s c_V \tag{47}$$

Total heat conductivities are calculated from species heat conductivities in a way similar to calculating total viscosity from species viscosities,

$$\kappa = \sum_{s=1}^{5} \frac{y_s \kappa_s}{\phi_s} \tag{48}$$

$$\kappa_V = \sum_{s=1}^{5} \frac{y_s \kappa_{Vs}}{\phi_s} \tag{49}$$

In equations (45) to (49),

$$\phi_s = \sum_r y_r \left[1 + \sqrt{\frac{\mu_s}{\mu_r}}\left(\frac{M_r}{M_s}\right)^{1/4}\right]^2 \left[\sqrt{8\left(1+\frac{M_s}{M_r}\right)}\right]^{-1}$$

The diffusion coefficient is determined by assuming a constant Lewis number,

$$D_s = \frac{\kappa L_e}{\rho c_p} \text{(Neutral heavy species, } L_e = 1.4) \tag{50}$$

4.3 Chemical reactions

For the five species air, there exist five reactions: three dissociation reactions for diatomic species and two exchange reactions.

$$
\begin{aligned}
&N_2 + M \rightleftharpoons 2N + M \\
&O_2 + M \rightleftharpoons 2O + M \\
&NO + M \rightleftharpoons N + O + M \\
&N_2 + O \rightleftharpoons NO + N \\
&NO + O \rightleftharpoons O_2 + N
\end{aligned}
$$

In dissociation reactions, M stands for a generic particle that acts as a collision partner in the reaction.

Rates for each reaction are calculated using the following formula,

$$
\begin{aligned}
R_1 &= \sum_m \left[-k_{f_1 m} \frac{\rho_{N_2}}{M_{N_2}} \frac{\rho_m}{M_m} + k_{b_1 m} \frac{\rho_N}{M_N} \frac{\rho_N}{M_N} \frac{\rho_m}{M_m} \right] \\
R_2 &= \sum_m \left[-k_{f_2 m} \frac{\rho_{O_2}}{M_{O_2}} \frac{\rho_m}{M_m} + k_{b_2 m} \frac{\rho_O}{M_O} \frac{\rho_O}{M_O} \frac{\rho_m}{M_m} \right] \\
R_3 &= \sum_m \left[-k_{f_3 m} \frac{\rho_{NO}}{M_{NO}} \frac{\rho_m}{M_m} + k_{b_3 m} \frac{\rho_N}{M_N} \frac{\rho_O}{M_O} \frac{\rho_m}{M_m} \right] \\
R_4 &= -k_{f_4} \frac{\rho_{N_2}}{M_{N_2}} \frac{\rho_O}{M_O} + k_{b_4} \frac{\rho_{NO}}{M_{NO}} \frac{\rho_N}{M_N} \\
R_5 &= -k_{f_5} \frac{\rho_{NO}}{M_{NO}} \frac{\rho_O}{M_O} + k_{b_5} \frac{\rho_{O_2}}{M_{O_2}} \frac{\rho_N}{M_N}
\end{aligned}
$$

Chemical reaction source terms are obtained from reaction rates as,

$$
\begin{cases}
\omega_{N_2} = M_{N_2}(R_1 + R_4) \\
\omega_{O_2} = M_{O_2}(R_2 - R_5) \\
\omega_{NO} = M_{NO}(R_3 - R_4 + R_5) \\
\omega_N = M_N(-2R_1 - R_3 - R_4 - R_5) \\
\omega_O = M_O(-2R_2 - R_3 + R_4 + R_5)
\end{cases} \tag{51}
$$

4.4 Models of reaction rate coefficients

The forward and backward reaction rate coefficients are defined based on translation temperature, and vibration temperature. Specifically, the following four models have been implemented,

- Park's model 1 [24]
- Dunn & Kang's model [25]
- Park's model 2 [26]
- Park's model 3 [27]

In Park's models, the forward and backward reaction rate coefficients have the form of

$$k_f\left(\overline{T}\right) = C_f \overline{T}^{\eta_f} \exp\left(-\theta_f / \overline{T}\right) \tag{52}$$

$$k_b\left(T\right) = \frac{k_f(T)}{k_{eq}(T)} \tag{53}$$

For dissociation reactions, $\overline{T} = \sqrt{TT_V}$ or $\overline{T} = T^{0.7}T_V^{0.3}$. While $\overline{T}$ is equal to translation temperature for exchange reactions. The backward reaction rate coefficients for all reactions are only defined on the translation temperature. For different Park's model, the parameters in Eq. (52) and the formula of equilibrium constant (k_{eq}) are different.

For Park's model 1, the formula of equilibrium constant is as follows,

$$k_{eq} = \exp(a_1 + a_2 z + a_3 z^2 + a_4 z^3 + a_5 z^4) \tag{54}$$

where $z = 10000/T$. Table 9 lists the parameters used in Eq. (54) for each reaction. The parameters in Eq. (52) are listed in Table 10.

Table 9. Parameters for equilibrium constant in Park's model 1

Reaction	a_1	a_2	a_3	a_4	a_5
1	3.898	-12.611	0.683	-0.118	0.006
2	1.335	-4.127	-0.616	0.093	-0.005
3	1.549	-7.784	0.228	-0.043	0.002
4	2.349	-4.828	0.455	-0.075	0.004
5	0.215	-3.657	0.843	-0.136	0.007

Table 10. Parameters for forward reaction rate coefficients in Park's model 1

Reaction	Partner	C_f (m^3/kg s)	η_f	θ_f (K)
1	N2	3.700e+15	-1.600	113200
	O2	3.700e+15		
	NO	3.700e+15		
	N	1.110e+16		
	O	1.110e+16		
2	N2	2.750e+13	-1.000	59500
	O2	2.750e+13		
	NO	2.750e+13		
	N	8.250e+13		
	O	8.250e+13		
3	N2	2.300e+11	-0.500	75500
	O2	2.300e+11		
	NO	2.300e+11		
	N	4.600e+11		
	O	4.600e+11		
4	-	3.180e+7	0.100	37700
5	-	2.160e+2	1.290	19220

For Park's model 2, the formula of equilibrium constant is as follows,

$$k_{eq} = \exp(a_1 + a_2 \ln z + a_3 z + a_4 z^2 + a_5 z^3) \tag{55}$$

where $z = 10000/T$. Table 11 lists the parameters used in Eq. (55) for each reaction. The parameters in Eq. (52) are the same as those listed in Table 10.

Table 11. Parameters for equilibrium constant in Park's model 2

Reaction	a_1	a_2	a_3	a_4	a_5
1	1.858	-1.325	-9.856	-0.174	0.008
2	2.855	0.988	-6.181	-0.023	-0.001
3	0.792	-0.492	-6.761	-0.091	0.004
4	1.066	-0.833	-3.095	-0.084	0.004
5	-2.063	-1.480	-0.580	-0.114	0.005

For Park's model 3, the formula of equilibrium constant is as follows,

$$k_{eq} = \exp(a_1 z^{-1} + a_2 + a_3 \ln z + a_4 z + a_5 z^2) \tag{56}$$

where $z = 10000/T$. Table 12 lists the parameters used in Eq. (56) for each reaction. The parameters in Eq. (52) are listed in Table 13.

Table 12. Parameters for equilibrium constant in Park's model 3

Reaction	a_1	a_2	a_3	a_4	a_5
1	1.606	1.5732	1.3923	-11.533	-0.004543
2	0.64183	2.4253	1.9026	-6.6277	0.035151
3	0.63817	0.68189	0.66336	-7.5773	-0.011025
4	0.967940	0.891310	0.7291	-3.9555	0.006488
5	-0.003732	-1.7434	-1.2394	-0.94952	-0.046182

Table 13. Parameters for forward reaction rate coefficients in Park's model 3

Reaction	Partner	C_f (m^3/kg s)	η_f	θ_f (K)
1	N2	7.00e+15	-1.600	113200
	O2	7.00e+15		
	NO	7.00e+15		
	N	3.00e+16		
	O	3.00e+16		
2	N2	2.00e+15	-1.500	59500
	O2	2.00e+15		
	NO	2.00e+15		
	N	1.00e+16		
	O	1.00e+16		
3	N2	5.00e+9	0.000	75500
	O2	5.00e+9		
	NO	1.10e+11		
	N	1.10e+11		
	O	1.10e+11		
4	-	6.40e+11	-1.000	38400
5	-	8.40e+6	0.000	19450

For Dunn & Kang's model, the forward reaction rate coefficient is calculated by formula similar to Eq. (52). However, the backward reaction rate coefficient is calculated using the following equation, with considering the equilibrium constant.

$$k_b(T) = C_b T^{\eta_b} \exp(-\theta_b / T) \tag{57}$$

The parameters in Eqs. (52) and (57) are listed in Table 14.

Table 14. Parameters for reaction rate coefficients in Dunn & Kang's model

Reaction	Partner	C_f (m^3/kg s)	η_f	θ_f (K)	C_b (m^3/kg s)	η_b	θ_b (K)
1	N2	4.70e+11	-0.5	113000	2.72e+4	-0.5	0
	O2	1.90e+11			1.10e+4		
	NO	1.90e+11			1.10e+4		
	N	4.085e+16	-1.5		2.27e+9	-1.5	
	O	4.085e+16			2.27e+9		
2	N2	7.20e+12	-1.0	59500	6.00e+3	-0.5	0
	O2	3.24e+13			2.70e+4		
	NO	3.60e+12			3.00e+3		
	N	3.60e+12			3.00e+3		
	O	9.00e+13			7.50e+4		
3	N2	3.90e+14	-1.5	75500	1.00e+8	-1.5	0
	O2	3.90e+14			1.00e+8		
	NO	7.80e+14			2.00e+8		
	N	7.80e+14			2.00e+8		
	O	7.80e+14			2.00e+8		
4	-	7.00e+7	0.0	38000	1.56e+7	0.0	0
5	-	3.20e+3	1.0	19700	1.30e+4	1.0	3580

4.5 Energy relaxation

In two temperature model, energy relaxation only happens between translation energy and vibration & electron energy, which can be expressed as

$$Q_{T-v,s} = \rho_s \frac{e_{vs}^*(T) - e_{vs}}{\tau_{vs}} \left| \frac{T_{shk} - T_{vs}}{T_{shk} - T_{vs,shk}} \right|^{S_s - 1} \tag{58}$$

where, $e_{vs}^*(T)$ is the vibration energy per unit mass of species s evaluated at the local translational temperature. The quantities T_{shk} and $T_{vs,shk}$ are the translational and vibration temperatures evaluated just behind the bow shock wave.

$$\tau_{vs} = \langle \tau_{s,L-T} \rangle + \tau_{cs} = \frac{\sum_r y_r}{\sum_r y_r / \tau_{sr,L-T}} + \frac{1}{a_s \sigma_v N_s} \qquad \left(a_s = \sqrt{\frac{8\bar{R}T}{\pi M_s}}\right)$$

$$\tau_{sr,L-T} = \frac{1}{p} \exp\left[A_{sr} \left(T^{-1/3} - 0.015 \mu_{sr}^{1/4} \right) - 18.42 \right] \text{ (p in atm)}$$

$$A_r = 1.16\times10^{-3}\,\mu_{sr}^{1/2}\theta_{vs}^{4/3} \qquad \mu_{sr} = M_s M_r \Big/ (M_s + M_r)$$

$$S_s = 3.5\exp\left(-\theta_s \Big/ T_{shk}\right) \qquad \sigma_v = 10^{-21}\left(50{,}000 \Big/ T\right)^2$$

Here, θ_s is a defined characteristic temperature.

5 Code validation and application

To validate the code, we have tested three cases of one- and two-dimensional hypersonic nonequilibrium flows, i.e.,

- Grossman et al.'s shock tube problem [28];
- Hornung's Nitrogen dissociation over 1 inch radius cylinder [29];
- Gnoffo's air flow over 1m radius cylinder;

For the shock tube problem, both the fifth-order WENO scheme and the second-order TVD scheme are used. However, only the WENO scheme is used for the other two cases. Viscous fluxes are calculated by a sixth-order central scheme. Time integration of the governing equations is obtained using explicit Runge-Kutta method.

5.1 One dimensional shock tube problem

A 1-D shock tube problem was studied by Grossman and Walters [28] to test their computer code on the simulation of nonequilibrium and reactive flows. Later, it was also considered by Meng-Sing Liou et al. [30]. The problem involves five species air at high temperature and pressure. The temperature and pressure ratios of driver section to driven section are 30 and 100, respectively. In current test, the shock tube is 1 m long. The problem is solved by a second-order TVD scheme and a fifth-order WENO scheme.

The initial flow conditions are:

$0 \le x \le 0.5\,\text{m}$: P = 100 atm, T = 9000 K, ρ = 2.641 kg/m^3

$0.5 \le x \le 1.0\,\text{m}$: P = 1 atm, T = 300 K, ρ = 1.1737 kg/m^3

In this test case, initial concentrations of five species equilibrium air are calculated based on Dunn & Kang's model [25] with constant pressure and constant temperature conditions. Densities of the mixture are exactly the same as those in Grossman and Walters' paper.

The following are simulation results at t=1.2d-4 second. Numerical simulation results are compared well with the exact real gas solution plotted in Grossman and Walters' paper.

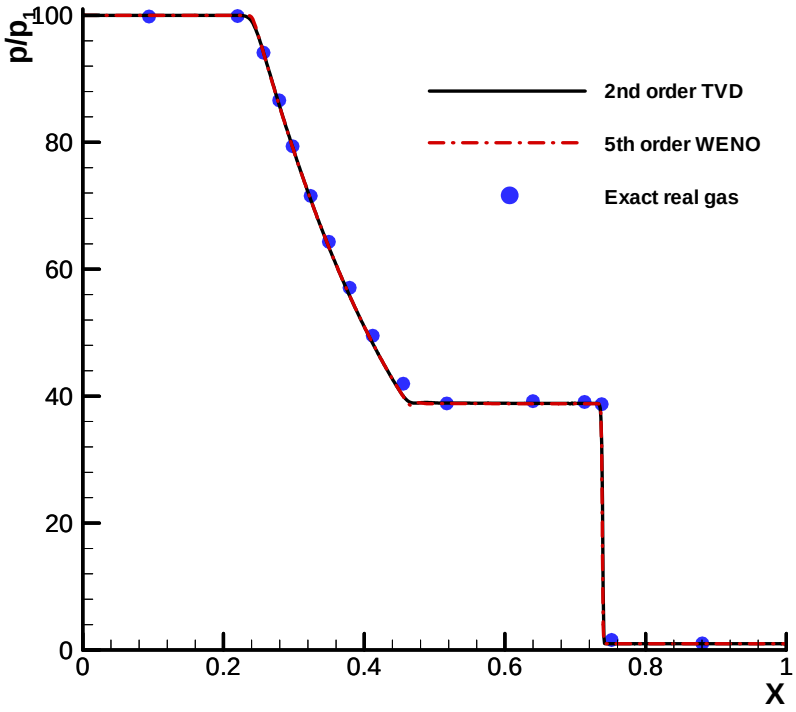

Figure 6. Pressure distribution along the shock tube

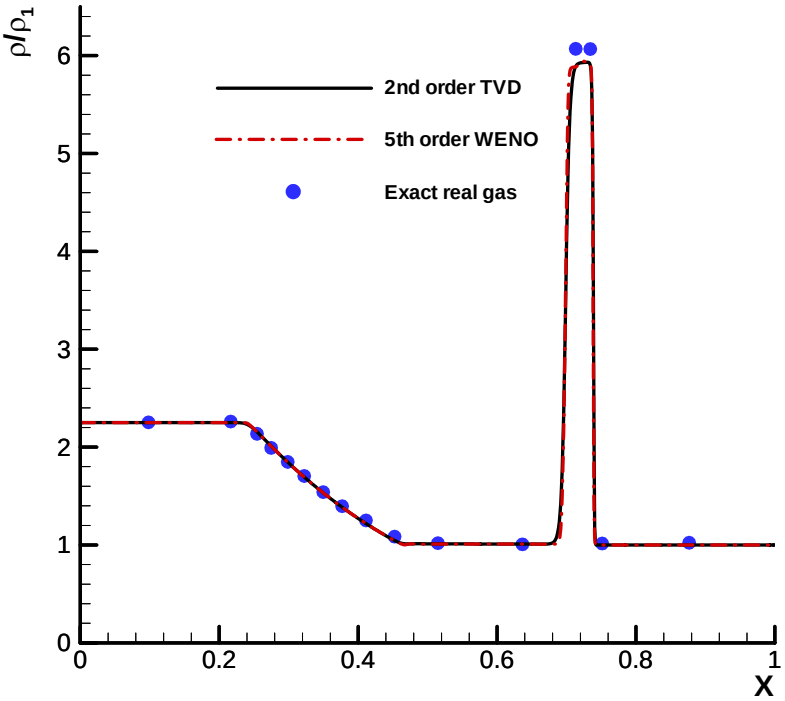

Figure 7. Density distribution along the shock tube

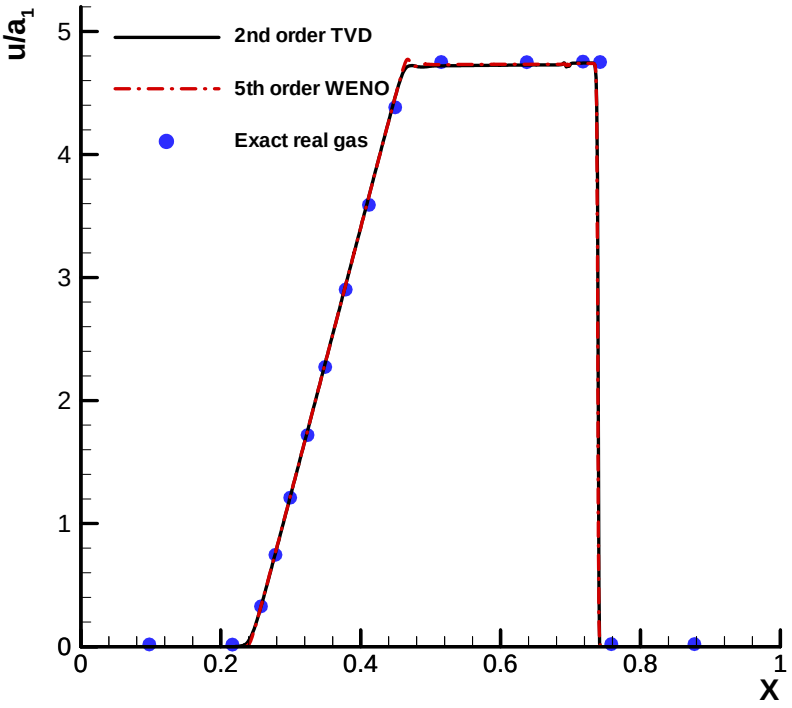

Figure 8. Velocity distribution along the shock tube

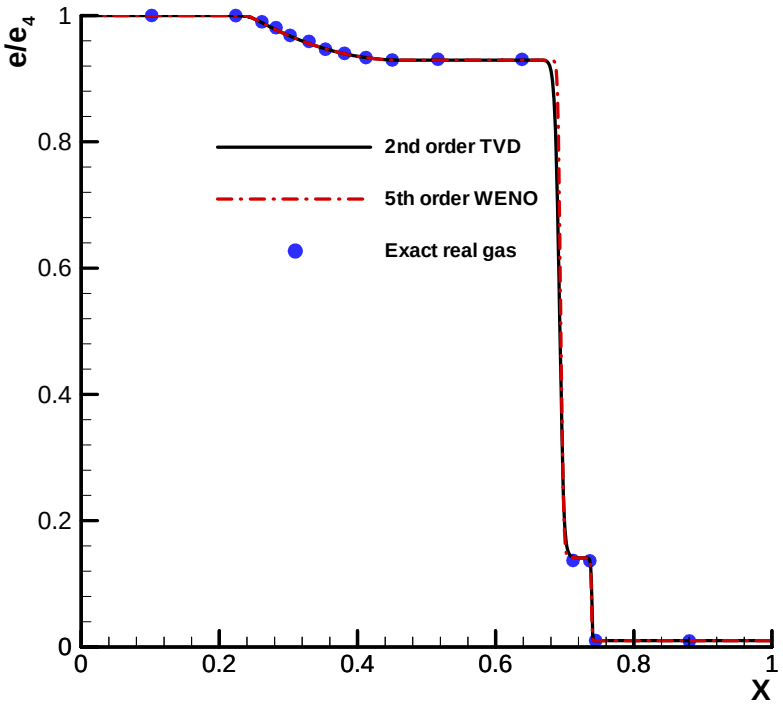

Figure 9. Specific energy distribution along the shock tube

Above figures show quite good agreements between our simulation results and the exact solution plotted in Grossman and Walters' paper. The only significant discrepancy happens in density of gas mixture between the shock and the contact surface. There density of numerical simulation is lower than that of exact solution. Similar discrepancy happened in Grossman and Walters' simulation results. Figure 9 is re-plotted by adding the density of Grossman and Walters' numerical simulation as shown in Fig. 10.

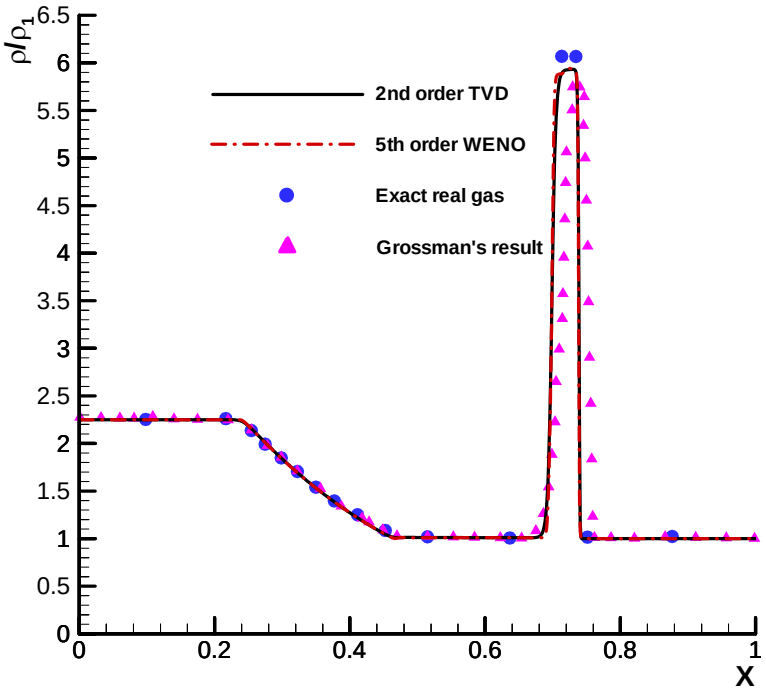

Figure 10. Molar Specific energy distribution along the shock tube (re-plotted)

The discrepancy in density might be caused by the numerical viscosity in finite difference scheme. Figure 10 shows that numerical viscosity in Steger-Warming scheme is much larger that those in current TVD scheme and WENO scheme. In all figures, the exact solution is obtained from the figure in Grossman and Walters' paper, which is calculated using Colella and Glaz's method [31].

5.2 Hornung's Nitrogen dissociation over 1 inch radius cylinder

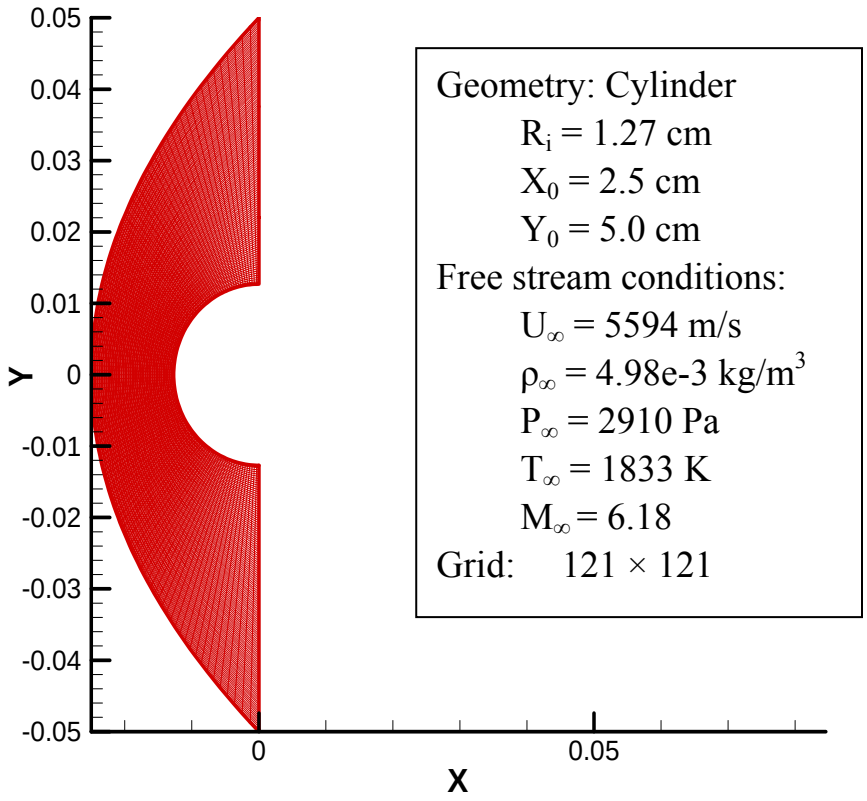

Figure 11. Geometry and free stream flow conditions

In order to check new implemented subroutines, the test process is divided into three steps:

1) Perfect gas flow. In this step, numerical simulation is conducted using original Jiang-Shu WENO scheme. The results are used as the standard solutions;

2) Perfect gas flow. Unlike the first step, here numerical simulation is conducted using new implemented Jiang-Shu WENO scheme and viscous flux subroutines for nonequilibrium flow (five species, two temperatures, viscosity and heat conductivity for gas mixtures). The temperature boundary condition on the cylinder is extrapolated. However, source terms are neglected. Here,

$$C_{N2} = 1.00,\ C_N = C_{O2} = C_{NO} = C_O = 0$$

3) Nonequilibrium flow with isothermal boundary condition.

For last three steps, the mass fractions of initial gas are

$$C_{N2} = 0.927,\ C_N = 0.073$$
$$C_{O2} = C_{NO} = C_O = 0$$

Comparisons of simulation results at steps 1 and 2 are shown in following two figures.

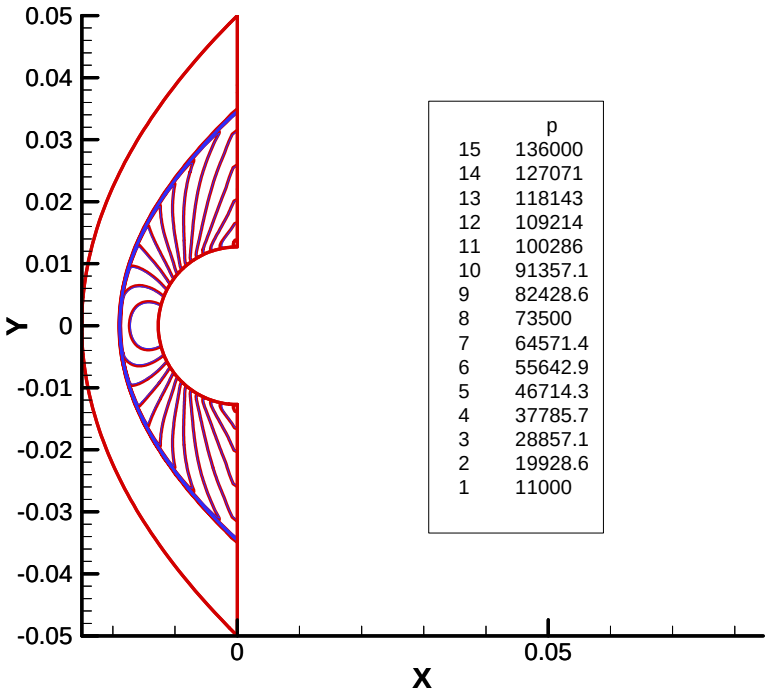

Figure 12. Pressure contours of steps 1 (red) and 2 (blue)

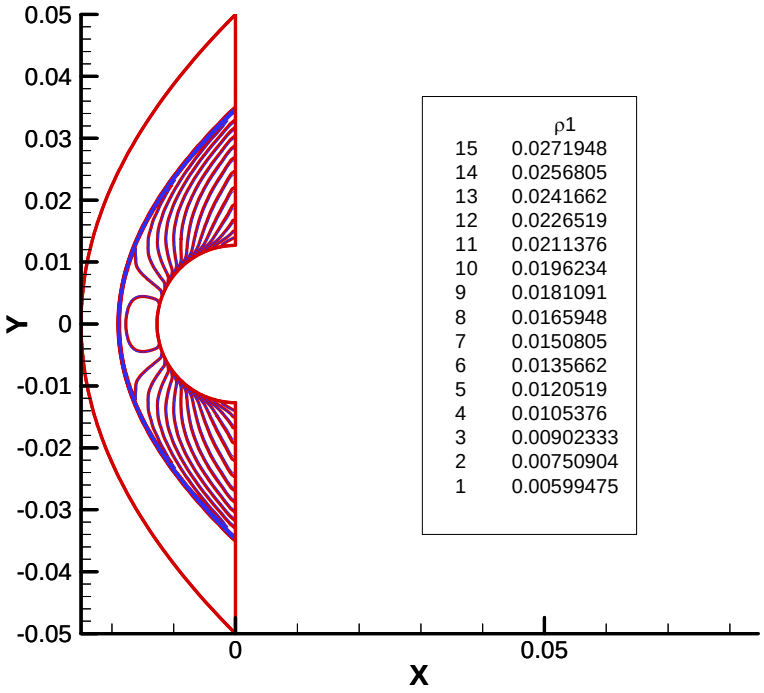

Figure 13. Density contours of steps 1 (red) and 2 (blue)

Figures 12 and 13 show pressure and density contours of simulations at steps 1 and 2. For both figures, blue contours stand for step 2 whereas red contours stand for step 1. Actually, the contours agree quite well. The good agreement between simulation results indicates that the new implemented inviscid and viscous subroutines are correct.

Figure 14 compares pressure contours of numerical simulations at steps 2 (green) and 3 (red). At step 3, chemical and thermal source terms are included. The figure shows that chemical reaction and thermal nonequilibrium dramatically decrease the shock standoff distance.

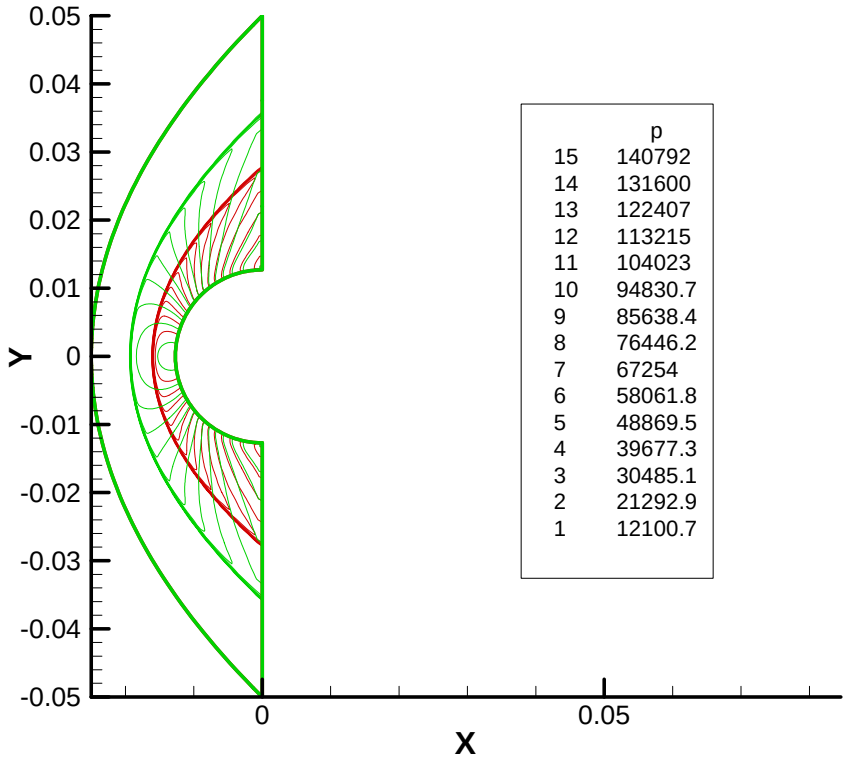

Figure 14. Pressure contours of steps 2 (green) and 3 (red)

To validate the simulation results of nonequilibrium flow, the results at step 3 are also compared with Hornung's experimental measurements as shown in the following three figures. The fringe number is calculated using the fomula,

$$F = \frac{(\rho - \rho_\infty) L (1.0 + 0.28 C_N)}{4160 \lambda} \tag{59}$$

In above equation, L is the geometrical path in experiment (0.1524 m), λ is the wavelength used for photograph (5.330^{-7} m), C_N is mass fraction of atomic Nitrogen. To

convert computational result to interferogram, the contours of constant fringe number, $\cos^2(\pi F)$, is plotted.

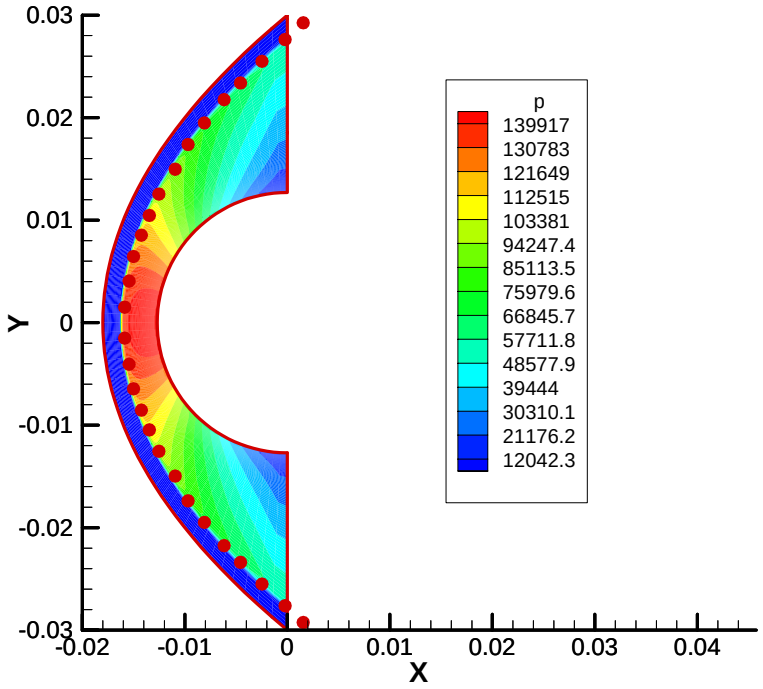

Figure 15. Comparison of shock standoff distance (Dots stands for experimental measurement).

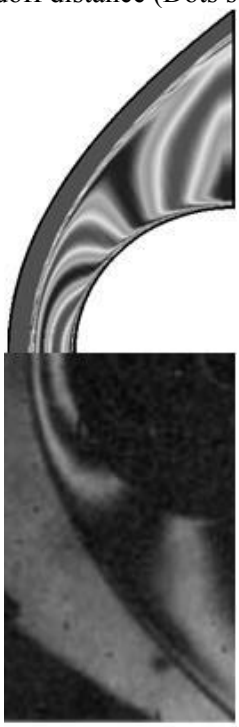

Figure 16. Comparison of fringe patterns (the lower half is experimental measurement).

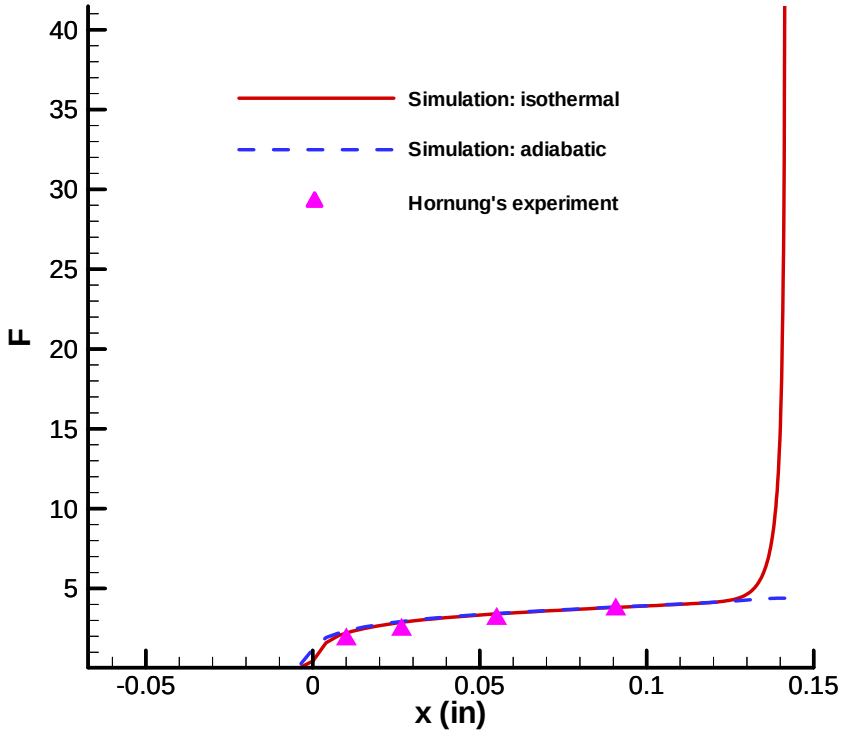

Figure 17. Quantitative comparison of fringe number.

As shown in figures 15 to 17, the shock standoff distance agrees well with experiment and the fringe pattern matches quite well with Hornung's experimental measurements. The test result on this case validated that the implementations of nonquilibrium and reactive flow solver to the ADPDIS3D code is correct.

5.3 Gnoffo's air flow over 1 m radius cylinder

Similar to section 5.2, the test scenario of this case is divided into three steps:

1) Perfect gas flow. In this step, numerical simulation is conducted using original Jiang-Shu WENO scheme. The results are used as the standard solutions;

2) Perfect gas flow. Numerical simulation is conducted using new implemented Jiang-Shu WENO scheme and viscous flux subroutines for non-equilibrium flow. The temperature boundary condition on the cylinder is extrapolated. However, source terms are neglected. To compared with the result of step 1, mass fractions are chosen as

$$C_{N2} = 1.00,\ C_N = C_{O2} = C_{NO} = C_O = 0$$

3) Nonequilibrium flow with isothermal boundary condition. The isothermal boundary conditions on the cylinder currently used are as follows,

$\frac{\partial c_s}{\partial \eta} = 0$, where c_s is mass fraction $\qquad \frac{\partial p}{\partial \eta} = 0$

u = v = w = 0, no-slip condition

The two temperatures on the cylinder are assigned to be equal to T_w (= 500 K). Total density is computed from pressure and translational temperature. Then species densities are calculated with total density and mass fraction. Total energy and vibration energy are calculated using species densities and two temperatures.

For steps 3 & 4, the mass fractions of initial gas are as follows,

$C_{N2} = 0.76$, $C_{O2} = 0.24$
$C_{NO} = C_N = C_O = 0$

To make the results comparable, all simulations are carried out on a 61 × 129 grid, exactly the same as what Gnoffo used in his simulation. Flow conditions and geometry are schematically shown below.

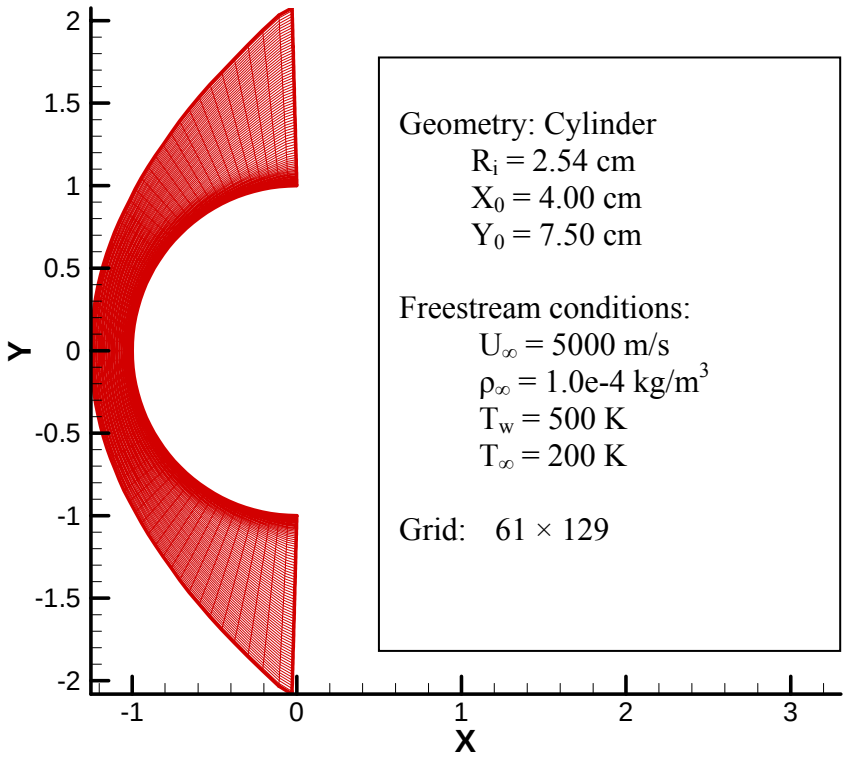

Figure 18. Geometry and free stream flow conditions.

Test results at steps 1 and 2 are neglected, because they are quite similar to what we get in section 5.2. The simulation results are also compared with Gnoffo's results obtained from Laura.

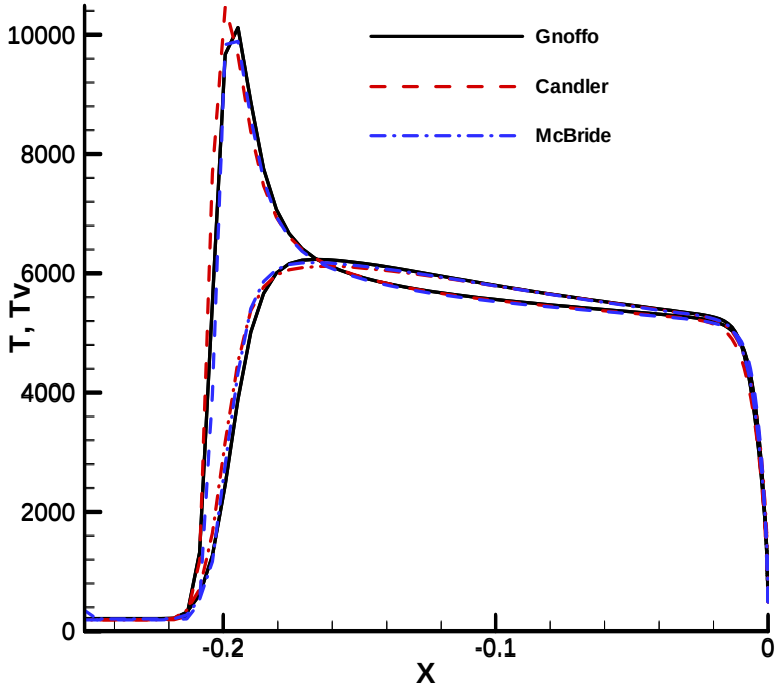

Figure 19. Comparison of temperature distributions along the stagnation line.

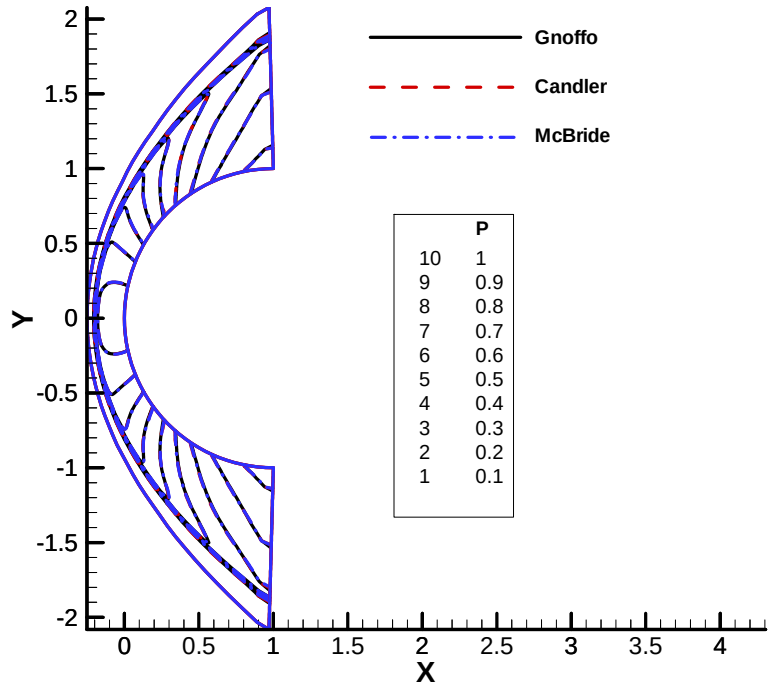

Figure 20. Comparison of pressure contours.

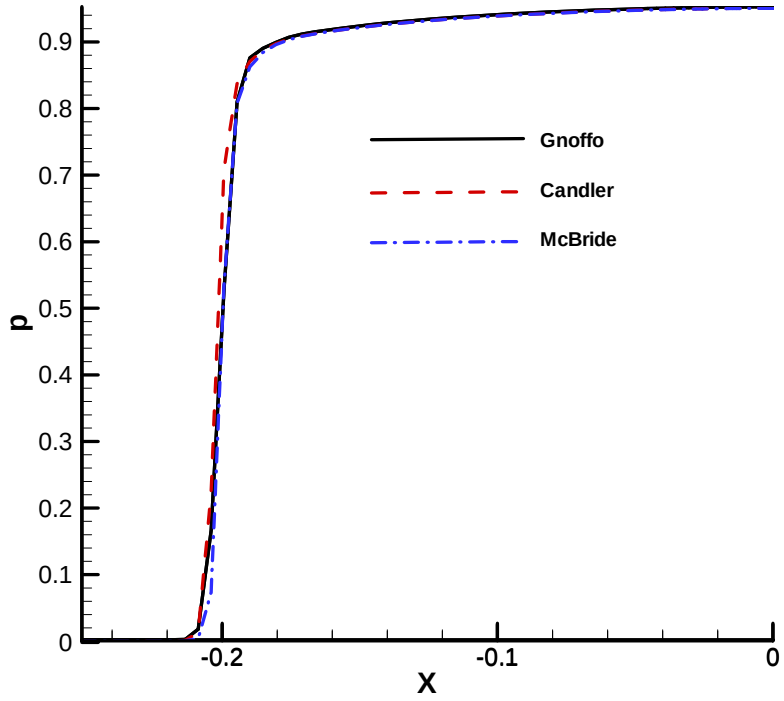

Figure 21. Comparison of pressure distributions along the stagnation line.

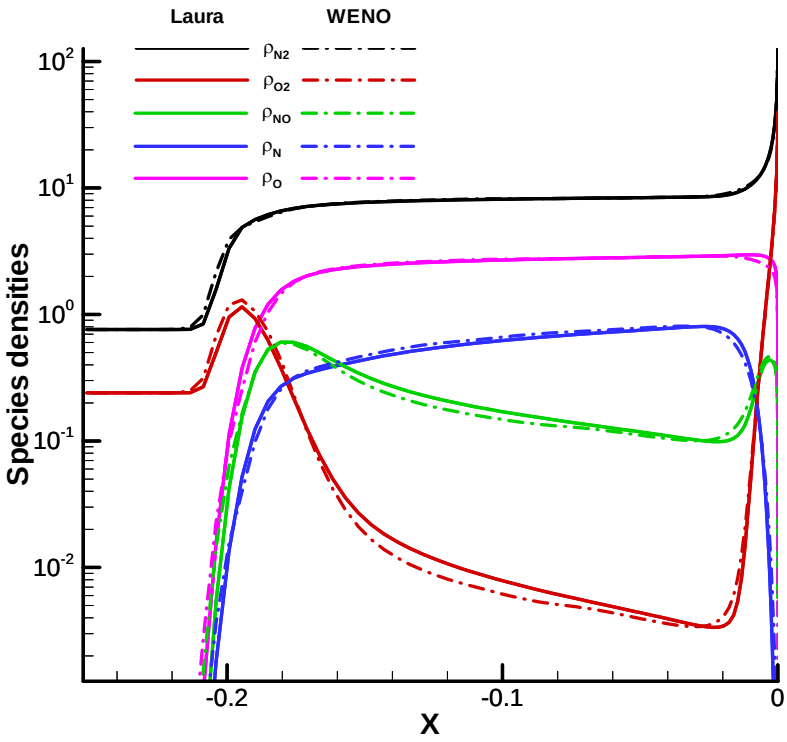

Figure 22. Comparison of species density distributions along the stagnation line

In figures 19 to 21, solid black line represents numerical simulation results of Gnoffo, obtained using the Laura code. The other two lines represent the results from the ADPDIS3D code using different models of vibration and electron energy. Dashed red line and Dashdotted blue line stands for the results using Candler's model and McBride's model, respectively. In Gnoffo's simulation, McBride's model is used.

These figures show that when McBride's model of vibration and electron energy is used, our simulation result with the ADPDIS3D code have a good agreement with Gnoffo's simulation based on Laura code. When Candler's model of vibration and electron energy is used, our results have visible differences with Gnoffo's result near the shock. The reason for the differences is that Candler's model of vibration and electron energy is too simple, only being accurate enough for low temperature. Figure 22 shows that the species density distributions along the stagnation line obtained from current WENO scheme have quite reasonal agreement with those obtained from Laura code. Again, the test results on this case validate that the implementations of nonquilibrium and reactive flow solver to the ADPDIS3D code is correct.

6. Summary

A CFD solver based on a fifth-order WENO scheme is developed for the simulation of nonequilibrium and reactive high-speed flows. The solver is implemented to the ADPDIS3D computer code package developed mainly by Yee and Bjorn, based on Park's two-temperature model. It is assumed that translation and rotation energy modes are in equilibrium at the translation temperature whereas vibration and electron energy modes are in equilibrium at the vibration temperature. The flow solver uses the fifth-order WENO scheme of Jiang and Shu with Roe's data reconstruction to model the inviscid fluxes. In order to validate the code, Yee's second-order TVD scheme is also implemented. Viscous fluxes are calculated by a sixth order central scheme. Time integration of the governing equations is obtained using explicit Runge-Kutta method. The code is validated by appling to numerical simulations of Grossman and Walters' shock tube problem, Hornung's Nitrogen dissociation problem over 1 inch radius cylinder, and a new problem of five species air over 1 meter radius cylinder. The results show that the WENO solver is accurately enough to simulate nonequilibrium and reactive hypersonic flows.

Acknowledgement

The work was mainly sponsored by a SciDAC Science Application Partnerships (SAP) in support of the DOE Turbulence Science Application program, monitored by Dr. Lali Chatterjee. The authors want to thank Dr. Helen C. Yee in NASA Ames Research Center and Dr. Bjorn Sjogreen in Lawrence Livermore National Lab for the collaborations on the SAP. The authors also appreciate Dr. Peter A. Gnoffo's help on running the five species air over 1 meter radius cylinder using LAURA code. The work was also

sponsored by by the AFOSR/NASA National Center for Hyersonic Research in Laminar-Turbulent Transition and by the Air Force Office of Scientific Research.

Reference

1. Anderson Jr., J.D., *Hypersonic and High Temperature Gas Dynamics*. 1998: McGraw-Hill.
2. Vincenti, W.G., and Kruger Jr., C. H., *Introduction to Physical Gas Dynamics* 1967: Krieger Publishing Co, INC.
3. Mannella, G.G., *Chemical Reactions in Electrical Plasmas.* The OHIO Journal of Science, 1966. **66**(3): p. 334-339.
4. Wright, M.J., Olejniczak, J., Walpot, L., Raynaud, E., Magin, T., Caillaut, L, and Hollis, B. R. , *A Code Calibration Study for Huygens Entry Aeroheating*. 2006, AIAA 2006-0382.
5. Gnoffo, P.A., Mccandless, R. S., and Yee, H. C., *Enhancements to Program LAURA for Computation of Three-Dimensional Hypersonic Flow* 1987, AIAA 1987-0280.
6. Gnoffo, P.A., *Computational Aerothermodynamics in Aeroassist Applications*. 2001, AIAA 2001-2623.
7. Gnoffo, P.A., *Computational Fluid Dynamics Technology for Hypersonic Applications*. 2003, AIAA 2003-3259.
8. Hash, D., Olejniczak, J, Wright, M. J., Dinish, P., Pulsonetti, M., Hollis, B. R., Gnoffo, P. A., Barnhard, M., Nompelis, I., and Candler, G., *FIRE II Calculations for Hypersonic Nonequilibrium Aerothermodynamics Code Validation: DPLR, LAURA, and US3D*. 2007, AIAA 2007-0605.
9. Wright, M.J.a.C., G. V., *A Data-Parallel Line Relaxation Method for the Navier-Stokes Equations*. 1997, AIAA 1997-2046.
10. Walpot, L., *Development and Application of a Hypersonic Flow Solver*. 2002, T. U. Delft University.
11. Yee, H.C., and Sjogreen, B., *Development of low dissipative high order filter schemes for multiscale Navier-Stokes/MHD systems.* Journal of Computational Physics 2007. **225**(1): p. 910-934.
12. Yee, H.C., and Sjogreen, B., *Nonlinear Filtering and Limiting in High Order Methods for Ideal and Non-ideal MHD.* Journal of Scientific Computing, 2006. **27**(1-3): p. 507 - 521.
13. Yee, H.C., and Sjogreen, B., *Efficient Low Dissipative High Order Schemes for Multiscale MHD Flows, II: Minimization of $\nabla \cdot B$ Numerical Error.* Journal of Scientific Computing, 2006. **29**(1): p. 115 - 164.
14. Sjogreen, B., and Yee, H.C., *Multiresolution Wavelet Based Adaptive Numerical Dissipation Control for High Order Methods.* Journal of Scientific Computing, 2004. **20**(2): p. 211 - 255.
15. Yee, H.C., and Sjogreen, B., *Designing Adaptive Low-dissipative High Order Schemes for Long-time Integrations*, in *Turbulent Flow Computation*, D. Drikakis, and Geurts, B., Editor. 2001, Springer Netherlands. p. 141-198.

16. Yee, H.C., Vinokur, M., and Djomehri, M. J. , *Entropy splitting and numerical dissipation.* Journal of Computational Physics 2000. **162**(1): p. 33 - 81.
17. Yee, H.C., Sandham, N. D., and Djomehri, M. J. , *Low-dissipative high-order shock-capturing methods using characteristic-based filters.* Journal of Computational Physics 1999. **150**(1): p. 33 - 81.
18. Park, C., *Assessment of two-temperature kinetic model for ionizing air.* Journal of thermophysics and heat transfer, 1989. **3**(3): p. 233-244.
19. Jiang, G.-S., and Shu, C-W., *Efficient Implementation of Weighted ENO Schemes.* Journal of Compuational Physics, 1996. **126**: p. 202-228.
20. Gnoffo, P.A., Gupta, R. N., and Shinn, J. L., *Conservation equations and physical models for hypersonic air flows in thermal and chemical nonequilibrium*. 1989, NASA Technical Paper 2867.
21. Yee, H.C., *A class of high-resolution explicit and implicit shock-capturing methods*. 1989, NASA Technical Momorandum 101088.
22. Candler, G.V., *The computation of weakly ionized hypersonic flows in thermo-chemical nonequilibrium*. 1988, Stanford University.
23. McBride, B.J., and Gordon, S., *Fortran IV program for calculation of thermodynamic data*. 1967, NASA TN D-4097.
24. Park, C., *On convergence of computation of chemically reacting flows*. 1985, AIAA paper 1985-0247.
25. Dunn, M.G., and Kang, S-W., *Theoretical and experimental studies of reentry plasmas*. 1973, NASA CR-2232.
26. Park, C., *Convergence of computation of chemical reacting flows.* Progress in Astronautics and Aeronautics, 1985. **103**: p. 478-513.
27. Park, C., *Nonequilibrium hypersonic aerothermodynamics*. 1990, New York: Wiley. .
28. Grossman, B., and Walters, R. W., *An analysis of flux-split algorithms for Euler's equations with real gas*. 1987, AIAA paper 1987-1117.
29. Hornung, H.G., *Non-equilibrium dissociating nitrogen flow over spheres and circular cylinders.* Journal of Fluid Mechanics, 1972. **53**(1): p. 149-176.
30. Liou, M.-S., Van Leer, B., and Shuen, J-S., *Splitting of inviscid fluxes for real gases.* Journal of Compuational Physics, 1990. **87**(1): p. 1-24.
31. Colella, P., and Glaz, P. M., *Efficient solution algorithms for the Riemann problem for real gases.* Journal of Compuational Physics, 1985. **59**: p. 264-289.